# Variability in the temperature structure around the tropical tropopause and its relationship with convective activity

Eriko Nishimoto

A dissertation submitted in partial fulfillment of
the requirements for the degree of

Doctor of Philosophy

Division of Earth and Planetary Sciences,
Graduate School of Science, Kyoto University
January 2013

## Abstract

Temperature around the tropical tropopause is one of the most important factors controlling the aridity of air in the stratosphere. Low temperatures generally occur to the east of tropical active convection around the equator and to the west in the subtropics, forming a horseshoe-shaped structure. This structure resembles a stationary wave response known as the Matsuno–Gill pattern, which is induced by the heating generated by the convective activities. This study investigates the variability of the horseshoe-shaped temperature structure and its relationship with the convective activities by using contemporary reanalysis and outgoing longwave radiation (OLR) data.

An index characterizing the horseshoe-shaped structure is established to quantitatively capture its variability. This index reveals the significant relationship with convective activities in the three monsoon regions with the seasonal and interannual timescales: the South Asian monsoon and the North Pacific monsoon areas during the northern summer and the Australian monsoon area during the southern summer. During the southern summer the horseshoe-shaped structure index is also related to convective anomalies associated with the El Niño-Southern Oscillation cycle, shifting eastward in El Niño years. With the intraseasonal oscillation (ISO), various types of eastward-propagating features are observed in the unfiltered OLR field during the southern summer. Cluster analysis is performed according to the propagation features of the convective activity. Each cluster shows different features in the distribution of sea surface temperature. The horseshoe-shaped temperature structure propagates eastward accompanied by the convective activity, and both the ISO life cycle and event-to-event variation are significantly correlated. The strength and location of the 100-hPa temperature minima are found to be different among the clusters. These results imply that the different ISOs will have different impacts on the dehydration process depending on their types.

# Contents

# List of Figures

# List of Tables

# Chapter 1

# Introduction

## 1.1 Tropical Tropopause Layer

### 1.1.1 General Feature

The tropical tropopause layer (TTL) has been considered as a transition layer between the troposphere and the stratosphere. In Figure 1.1 several aspects of the TTL are illustrated. The traditional tropopause defined by the World Meteorological Organization lapse rate criterion or the cold point tropopause is located at ∼100 hPa and the stratospheric mean upwelling occurs above ∼70 hPa, while the top of convection is usually situated below 150 hPa in the tropics. A level of zero radiative heating in the clear-sky condition is also located around this altitude.

The TTL is an important region from the viewpoint of stratosphere-troposphere exchange (STE), because the TTL is a passage from the troposphere to the stratosphere for mass and chemical species which affect stratospheric air condition. In particular, the amount of water vapor transported into the stratosphere is controlled to a high degree by the tropical tropopause temperatures; *Brewer* [1949] suggested that the extreme dryness of the stratosphere is due to a global-scale circulation originating in the Tropics, wherein air entering the stratosphere is freeze dried when crossing the cold tropical tropopause. Striking confirmation of this relationship is provided by

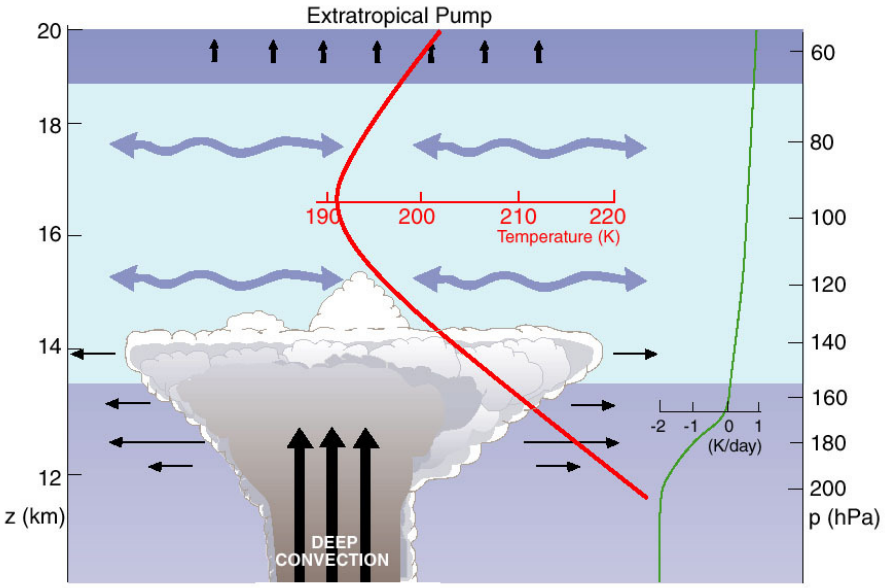


Fig. 1.1 A schematic diagram of the TTL. The top of large scale convective out flow in the tropics is usually situated below 14 km, while the traditional tropopause defined by the thermal structure is located around 16.5 km. Upwelling of the stratospheric pump in the lower stratosphere occurs above 19 km. A level of zero radiative heating in the clear-sky condition is found around 13km (green line). From http://www.atmos.washington.edu/academic/midatmos.html.

the observed annual cycle in stratospheric water vapor coupled to the annual cycle in tropical temperatures (the tropical "tape recorder", *Mote et al.* [1996]).

### 1.1.2 Dehydration Process

Stratospheric water vapor contributes to the radiative balance of the stratosphere and influences variability and recovery of the ozone layer through its radiative and photochemical nature [*Kley et al.*, 2000]. Water vapor variations in the tropical lower stratosphere have been investigated on intraseasonal [e.g., *Fujiwara et al.*, 2001; *Eguchi and Shiotani*, 2004], seasonal [e.g., *Mote et al.*, 1996; *Randel et al.*, 2001], and inter-annual time scales such as quasi-biennial oscillation (QBO) [e.g., *Niwano*, 2003; *Fuji-*

*wara et al.*, 2010] and El Niño-Southern Oscillation (ENSO) [e.g., *Randel et al.*, 2004; *Fueglistaler and Haynes*, 2005]. As for the longer-term change, increasing trends of stratospheric water vapor have been reported at Boulder (40.0°N, 105.25°W) [*Oltmans et al.*, 2000; *Rosenlof et al.*, 2001; *Scherer et al.*, 2008] and in the tropical lower stratosphere [*Fujiwara et al.*, 2010]. Around 2000–2001 a drop in lower stratospheric water vapor was observed both in the extra-tropical [*Scherer et al.*, 2008] and tropical [*Fujiwara et al.*, 2010] regions, and since then, persistent low values have been observed until at least 2005. Mechanisms responsible for the increasing trends during the past half-century and for the recent sudden drop are still unclear.

Water vapor concentration in the lower stratosphere is mainly controlled by the dehydration processes in the TTL. In order to understand the stratospheric water vapor amount and their variation, many hypotheses about the dehydration processes are proposed including the studies of cirrus formation [*Jensen*, 2004], the atmospheric waves such as the Kelvin waves [*Fujiwara et al.*, 2001; *Immler et al.*, 2008; *Fujiwara et al.*, 2009], and convective overshooting [*Sherwood and Dessler*, 2000]. *Holton and Gettelman* [2001] proposed the "cold trap" hypothesis and emphasized horizontal transport via a cold trap region. They showed in their two-dimensional (longitude-height) idealized model that significant dehydration occurs in the cold region if horizontally uniform easterly flow prevails in the TTL. This hypothesis was further examined by General Circulation Model (GCM) simulations (Figure 1.2) [*Hatsushika and Yamazaki*, 2003]. *Fueglistaler and Haynes* [2005] estimated the water vapor amount at the top of the TTL by using the Lagrangian temperature history along trajectories and demonstrated that the water vapor amount is determined as the minimum saturation water vapor mixing ratio along the pathway of the air parcel.

## 1.2 Tropical Tropopause Temperature

### 1.2.1 Horizontal Structure

*Newell and Gould-Stewart* [1981] surveyed the temperature distribution at 100 hPa

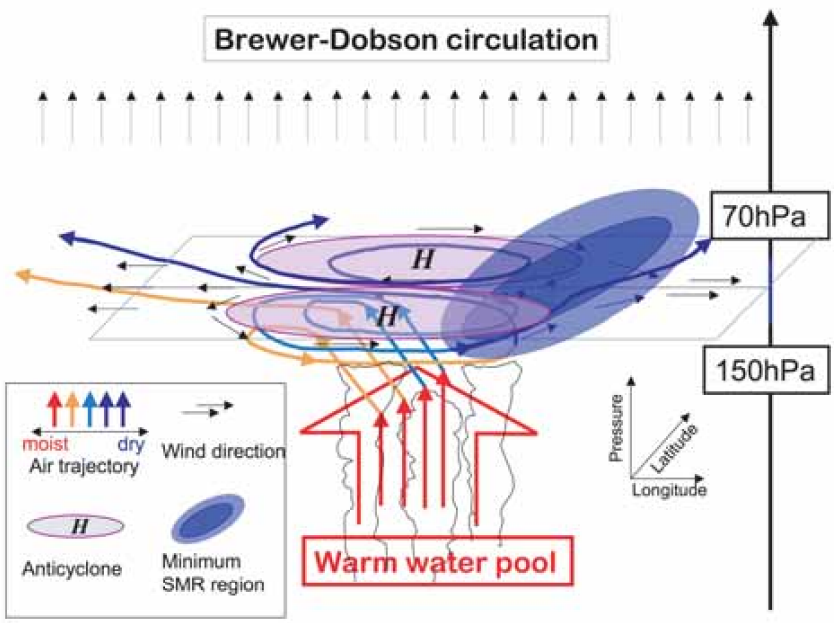


Fig. 1.2 Schematic picture for the path of the air from the troposphere to the stratosphere through the tropical tropopause layer. The color of each line denote the pressure level, and the shaded area corresponds to the minimum saturation mixing ratio region. The anticyclones around the tropopause are also drawn with purple lines. From *Hatsushika and Yamazaki* [2003].

using global data from a radiosonde network, and showed that temperatures lower than the zonal average are found over the Indian Ocean during the northern summer and over the western Pacific during the southern summer. Figure 1.3 shows the climatological temperature at 100 hPa adapted from *Nishi et al.* [2010]. In general the low temperatures occur over the western Pacific in the the tropics and extend northwestward and southwestward toward the subtropics, forming a horseshoe-shaped structure. The horseshoe-shaped structure is prominent, especially in the northern and southern summers, when convective activities are active over the Indian and western Pacific Ocean.

This horseshoe-shaped structure resembles the stationary wave response known as the Matsuno–Gill pattern. *Matsuno* [1966] investigated several equatorial wave modes in a shallow-water equation, and *Gill* [1980] showed that heating near the equator

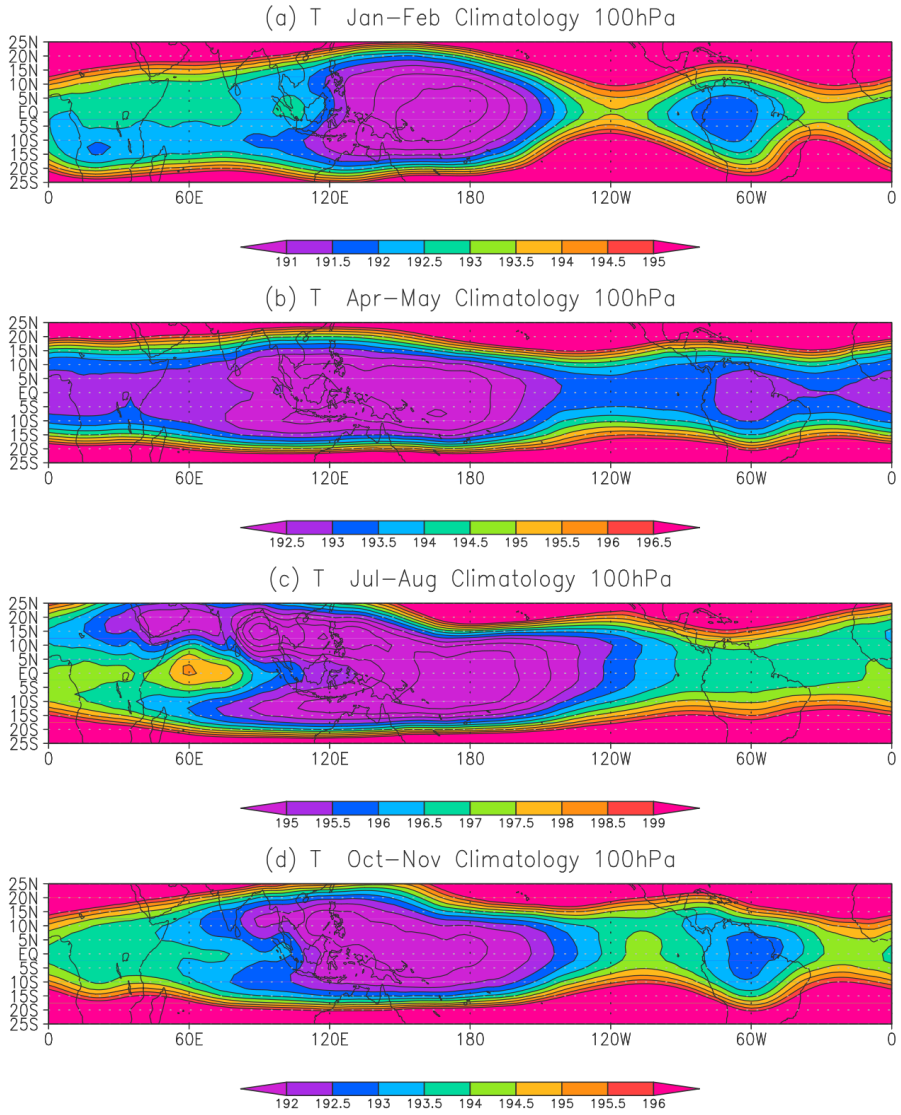


Fig. 1.3 Climatological (1979–2001) monthly mean temperature (K) at 100 hPa in (a) January–February, (b) April–May, (c) July–August, and (d) October–November (ERA-40). Contour interval is 0.5 K, and contours above (a) 195 K, (b) 196.5 K, (c) 199 K, and (d) 196 K are omitted. From *Nishi et al.* [2010].

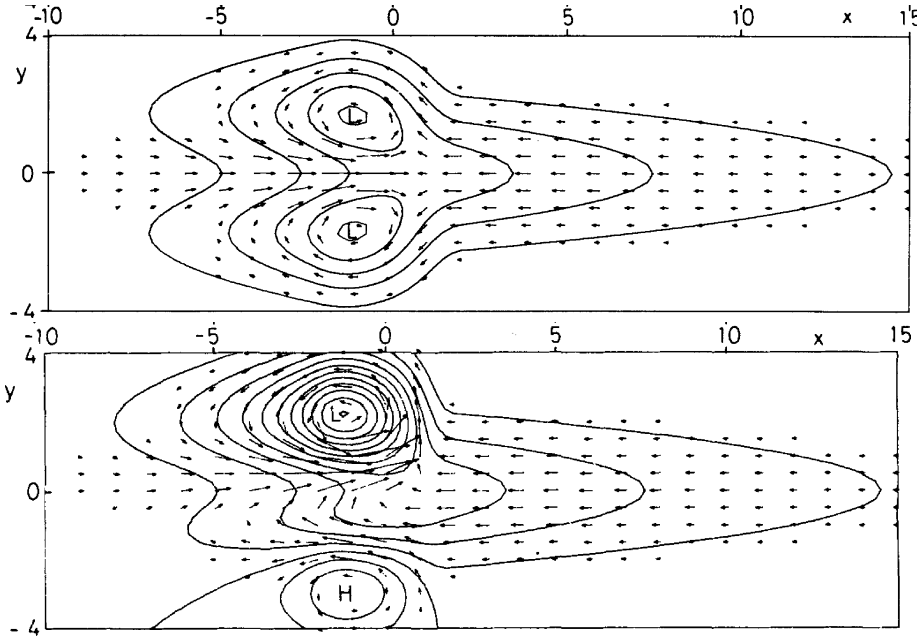


Fig. 1.4 Contours of perturbation pressure $p$ superimposed on the velocity field for the lower layer. Solutions for (top) heating symmetric about the equator in the region $\mid x \mid < 2$ and for (bottom) heating which is confined to the region $\mid x \mid < 2$ and is mainly concentrated to the north of the equator. From *Gill* [1980].

produces a characteristic wave structure in wind and pressure fields, which was later named the Matsuno–Gill pattern. Figure 1.4 shows the Matsuno–Gill pattern response induced by the heating which is located on the equator (top) and away from the equator (bottom). The Matsuno–Gill pattern can be described as a combined structure of two types: one is located in the eastern part and represents a Kelvin wave confined around the equator with no meridional velocity, and the other is in the western part and represents a Rossby wave with a pair of symmetric circulations in the subtropics. When the heating is located away from the equator, the Rossby response is vigorous in the hemisphere where the heating is located and is weakened in the opposite hemisphere.

The Matsuno–Gill response in the tropopause temperature has been demonstrated using multiple-layer models by *Highwood and Hoskins* [1998] and *Norton* [2006]. Fig-

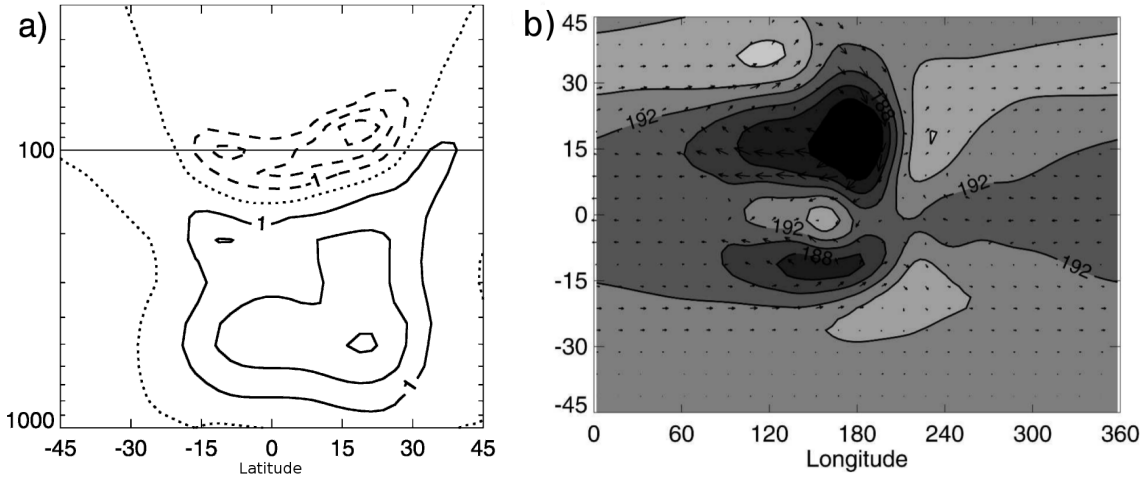


Fig. 1.5 (a) Zonal mean temperature response of the model with Gaussian heating centered at 15°N. Contour interval is 1 K and solid contours indicate positive values and dashed contours negative values; dotted is the zero contour. (b) Temperature and wind vectors at 100 hPa from the model with heating centered at 15°N. Contour interval is 2 K; darker shading indicates colder temperatures. From *Norton* [2006].

ure 1.5 presents the results of *Norton* [2006] with heating at 15°N; the heating has a Gaussian distribution in the horizontal and vertical with a peak at 180° longitude and 420 hPa, and it is identically zero above the 200-hPa level. The temperature anomaly responses at the most levels are vigorous above the regions of imposed heating. However the response at 100 hPa occurs in the both hemispheres with a secondary region of cold temperatures at 10°S. *Highwood and Hoskins* [1998] and *Norton* [2006] attributed the occurrence of the cold temperatures at 10°S in Figure 1.5 to a wave response.

*Highwood and Hoskins* [1998] and *Norton* [2006] also showed that wind and pressure fields have a corresponding pattern to satisfy the hydrostatic relationship; anticyclonic circulations exist in the upper troposphere subtropics, while cyclonic circulations in the lower troposphere subtropics. Using ECMWF 40-year reanalysis (ERA-40) data, *Dima and Wallace* [2007] estimated the annual-mean temperature fields in the trop-

ics from geopotential height data through the hypsometric equation, and found the horseshoe-shaped structure with low temperatures over the western Pacific in the 150–70 hPa layer. *Hatsushika and Yamazaki* [2003] investigated the transport process through the tropical tropopause in a GCM and revealed that the cold tropopause temperatures and the upper tropospheric circulations characterized by the Matsuno–Gill pattern play an important role in the dehydration process (Figure 1.2).

*Randel and Park* [2006] and *Park et al.* [2007] used National Centers for Environmental Prediction/National Center for Atmospheric Research (NCEP/NCAR) reanalysis and outgoing longwave radiation (OLR) data, and showed that low tropopause temperatures presented in the Eastern Hemisphere during the northern summer are coupled to convective activities over the Asian monsoon region. However, the spatial and temporal variability of the horseshoe-shaped structure and quantitative evaluation of its relationship with convective activities are not clear yet.

### 1.2.2 Vertical Structure

To investigated tropical temperature profiles around the TTL, *Nishi et al.* [2010] conducted analyses using data obtained by the global positioning system radio-occultation limb-sounding technique of the Constellation Observing System for Meteorology, Ionosphere, and Climate (COSMIC). We[*1] then detected that vertically thin inversion layers occur most frequently over the Indian Ocean around 60°E during the northern summer. Figure 1.6 presents the daily time sequence of the vertical temperature gradient along the equator at 14.5–15 km. The most pronounced feature is the continuous stable region around 30°E–70°E during the latter half of July and all of August. In this longitudinal range, inversion layers are frequently observed. Superposed on this stationary structure, an eastward–moving disturbance is also detected and it contributes to the time variability of vertical gradient in the region. For example, an area of large gradient value is detected at 20°E on 15 August and

[*1] Eriko Nishimoto was the second author in *Nishi et al.* [2010] and in charge of analyses using the COSMIC data.

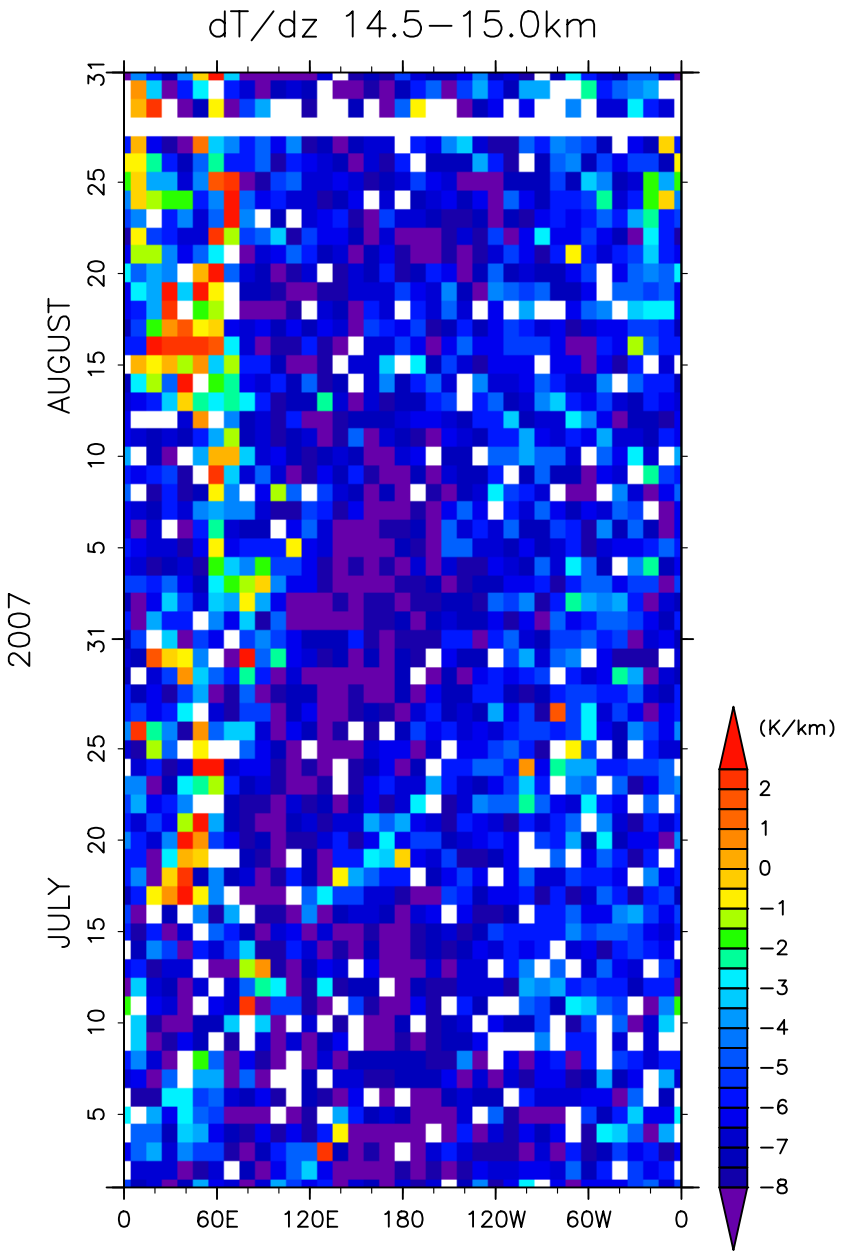


Fig. 1.6 Longitude–time section of the vertical temperature gradient averaged between 5°S and 5°N (K/km) between 14.5 and 15 km. From *Nishi et al.* [2010].

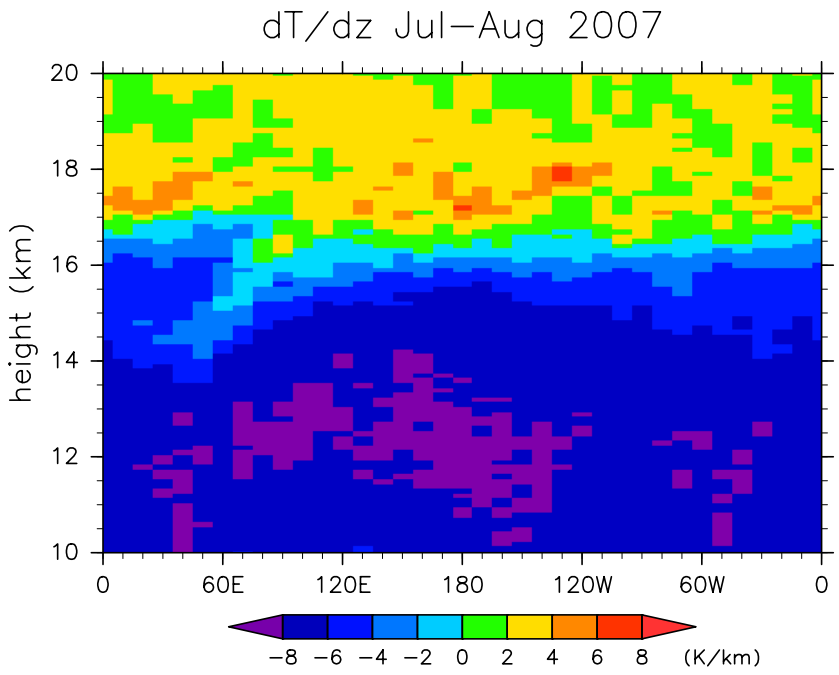


Fig. 1.7 Vertical temperature gradient averaged in July–August 2007 in the 2.5°S–2.5°N range. From *Nishi et al.* [2010].

moves eastward to reach 70°E on 24 August.

Figure 1.7 presents a longitude–height section of the vertical temperature gradient averaged over July–August 2007 around the equator in order to pick out only the stationary component. Cold point tropopause, which is shown as a zero line of vertical temperature gradient, is around 16.5 km height in all longitude range. A statically stable layer with vertical extent of 1 km or less is well detected around the Indian Ocean. At the 14.5–15 km level, a shallow stable layer is detected around 60°E. In the east, the layer rises to about 16 km around 100°E, where the shallow stable layer is connected to the stratospheric stable region. On the other hand, it goes down into the somewhat lower troposphere in the west, and it is located at 14 km at 50°E. To the west of 50°E, the stable layer is not clear.

The further analyses using the ERA-40 data for 23 years confirmed the presence of a warm anomaly that has a structure consistent with the stable layer detected

by COSMIC analysis; the warm anomaly is surrounded by the horseshoe-shaped low temperatures (Figure 1.3c). The magnitude of the warm anomaly was small in the El Niño years (1987 and 1997). However, mechanisms of the inversion layer and high temperatures remain unclear.

## 1.3 Variability in the Tropical Convective Activity

### 1.3.1 Seasonal Variability

Major convective activities occur in and adjacent to the Asian monsoon region during the northern summer and the Australian monsoon region during the southern summer. *Murakami and Matsumoto* [1994] showed that the Asian monsoon region is divided by the boundary over the South China Sea, where relatively dry weather persists. One region is located over the Bay of Bengal and is driven by thermal contrast between the Indian subcontinent and the Indian Ocean. The other is located over the western North Pacific, where the sea surface temperature is highest in the world, and is mainly driven by asymmetry in sea surface temperatures over the South China Sea and the western North Pacific. These two monsoon systems are called the Southern Asian monsoon (SoAM) and the North Pacific monsoon (NPM), respectively. The Australian monsoon (AUM) is located over northern Australia and mainly established by thermal contrast between the Australian continent and the Arafura Sea [*Hung and Yanai*, 2004, and references therein]. The domain of these three monsoon systems, SoAM, NPM, and AUM, is illustrated in Figure 1.8.

The Asian monsoons significantly impact on tracer distributions in the extratropical upper-troposphere and lower-stratosphere (UTLS) as evidenced by satellite data [*Park*, 2004; *Randel and Park*, 2006; *Fu et al.*, 2006; *Park et al.*, 2008] and aircraft measurements [*Schuck et al.*, 2010]. Monsoon circulations are associated with upward transport in persistent deep convection, together with large-scale anticyclonic circulations in the UTLS up to 70 hPa [*Dunkerton*, 1995]. An example of the chemical and dynamical signature of the Asian monsoon anticyclone is shown in Figure 1.9, high-

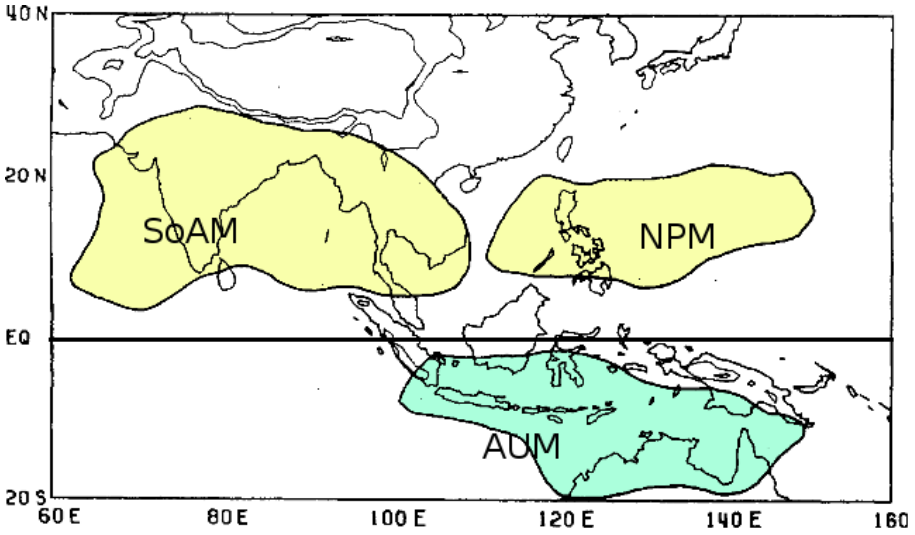


Fig. 1.8 The domains of the three monsoon systems, SoAM, NPM, and AUM. From *Murakami and Matsumoto* [1994].

lighting elevated mixing ratios of CO at 100 hPa coupled with the anticyclonic circulation at this level. Enhanced levels of CO (and also other tropospheric tracers [*Park et al.*, 2008; *Randel and Wu*, 2010]) occur within the monsoon anticyclone, resulting from the upward transport of surface pollution in deep convection and isolation of air within the strong anticyclonic circulation [*Park et al.*, 2009]. The anticyclonic circulation is also linked to persistent quasi-horizontal transport between the tropics and extratropics upstream and downstream of the anticyclone [*Gettelman*, 2004; *Konopka et al.*, 2009]. *Ploeger et al.* [2010] and *Konopka et al.* [2010] suggest a significant fraction of the air in the TTL originates from extratropics via this mechanism during the northern summer. From analysis of hydrogen cyanide (HCN) observations, there is also evidence that vertical transport in the monsoon circulation extends above the tropopause directly into the lowermost stratosphere and is entrained into the tropical Brewer-Dobson circulation [*Randel and Wu*, 2010], so that the Asian monsoon can have direct chemical influence on the global stratosphere.

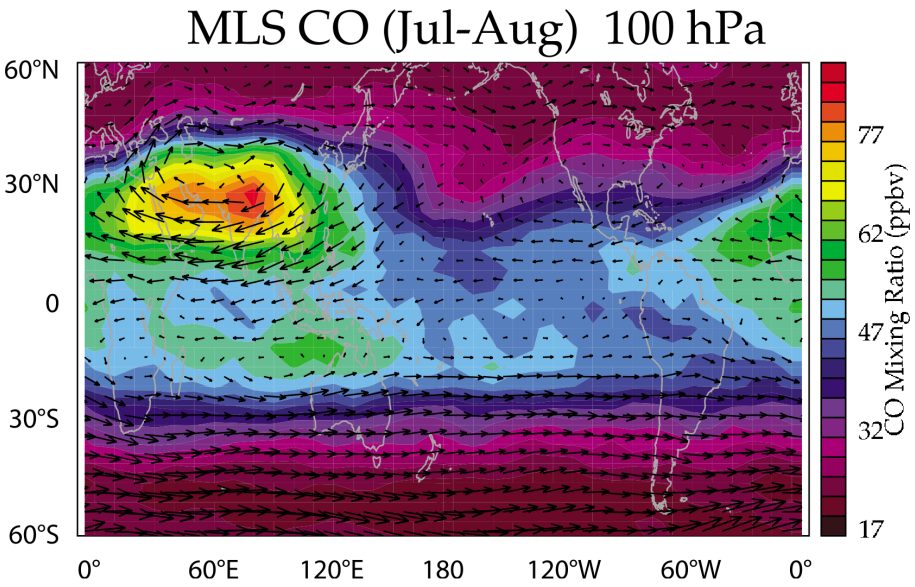


Fig. 1.9 Horizontal map of 100 hPa of July–August 2005 average Microwave Limb Sounder (MLS) CO (ppbv) and NCEP horizontal wind fields (vectors). Adapted from *Park et al.* [2007].

### 1.3.2 Interannual Variability

El Niño-Southern Oscillation (ENSO) is one of the most dominant interannual variations in the tropical atmosphere and ocean. Its effect is maximum during the southern summer, involving migration of convective activities [e.g., *Yulaeva and Wallace*, 1994; *Gettelman et al.*, 2001], which are stronger in La Niña years located over the western North Pacific than in El Niño years located over the eastern Pacific. During the northern summer, however, ENSO in the previous winter or spring affects convective activities in and adjacent to the Southeast Asia monsoon in the northern early summer [*Kawamura et al.*, 2001a] and to the North Pacific monsoon region throughout the northern summer [*Kawamura et al.*, 2001b] via the response of sea surface temperatures over the Indian Ocean.

The tropopause temperature could be also affected by the ENSO cycle. During the

El Niño phase, tropopause temperatures are fairly uniform; therefore, distribution of water vapor mixing ratios around the tropical tropopause is more zonally uniform than that during the La Niña phase [*Fueglistaler and Haynes*, 2005]. *Gettelman et al.* [2001] and *Fueglistaler and Haynes* [2005] reported that minimum and average tropopause temperatures do not significantly change in connection with the ENSO cycle, but strong El Niño rather than La Niña conditions create moistening.

### 1.3.3 Intraseasonal Variability

The Madden–Julian Oscillation (MJO), an eastward-propagating convective complex with a timescale of 30–60 days, is one of the most dominant disturbances in the tropical atmosphere [e.g., *Madden and Julian*, 1994; *Zhang*, 2005]. The schematic diagram of the MJO life cycle is illustrated in Figure 1.10. Its activities are most vigorous in the southern summer from the Indian Ocean to the western Pacific in the southern hemisphere [e.g., *Hendon et al.*, 1999; *Zhang*, 2005]. The vertical structure of the MJO extends well into the stratosphere [*Madden and Julian*, 1972; *Kiladis et al.*, 2005] and affects the zonally asymmetric temperature in the tropical tropopause [e.g., *Kiladis et al.*, 2001; *Suzuki and Shiotani*, 2008]. Using the global vertical temperature profiles from the Atmospheric Infrared Sounder (AIRS) and contemporary reanalyses, *Tian et al.* [2006, 2010] found that a Rossby and Kelvin wave pattern, which looks like the Matsuno–Gill pattern, appears in the temperature anomaly field at 100 hPa and propagates eastward with the deep convection anomaly associated with the MJO.

A possible influence of the MJO on the dehydration mechanism around the TTL was demonstrated by *Eguchi and Shiotani* [2004]. In their analysis of five MJO events in two southern summers (1991–1993), they observed a low water vapor mixing ratio and cirrus clouds at the 100-hPa level to the east of the convective anomaly as it propagated into the western Pacific. They attributed the occurrence of the cirrus clouds to the low temperatures produced by the convective system. As shown in Figure 1.11, the low temperatures form the equatorially symmetric horseshoe-shaped structure during the phase when the active convection anomaly is centered over the

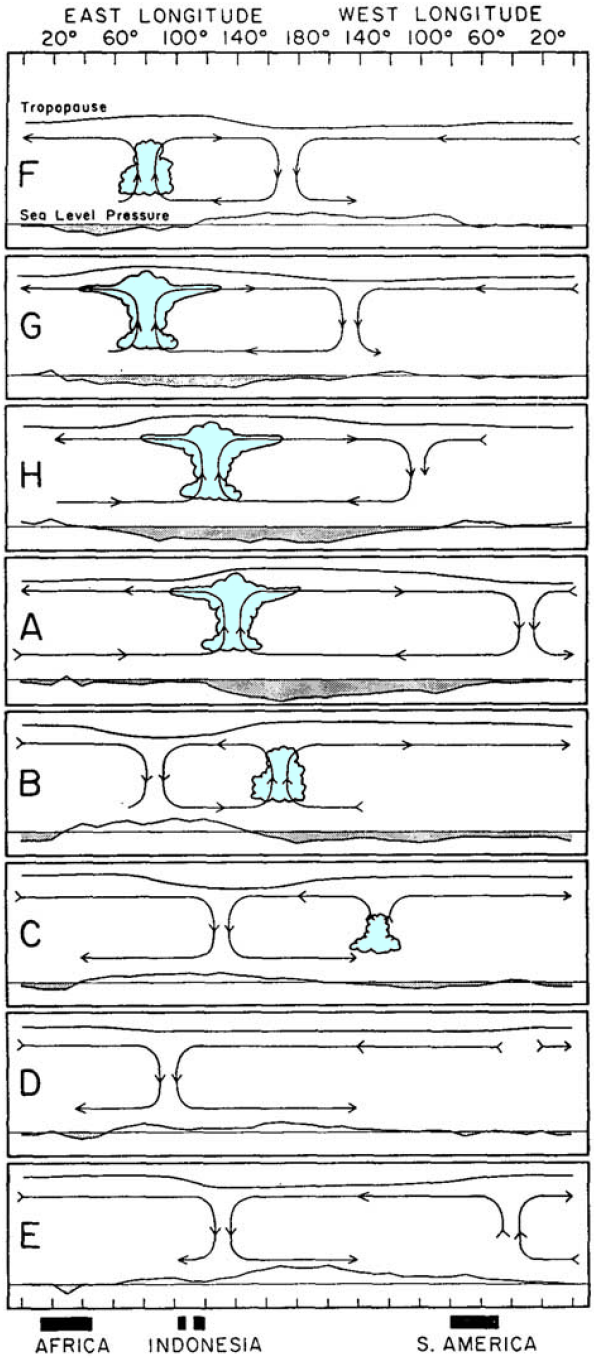


Fig. 1.10 Longitude-height schematic diagram along the equator illustrating the fundamental large-scale features of the MJO through its life cycle (from top to bottom). Cloud symbols represent the convective center, arrows indicate the zonal circulation, and curves above and below the circulation represent perturbations in the upper tropospheric and sea level pressure. From *Madden and Julian* [1972].

western Pacific. *Virts and Wallace* [2010] showed a map of the regression of 80-day high-pass filtered TTL cirrus clouds onto phases of the MJO index derived by *Wheeler and Hendon* [2004]; the MJO index is based on the first two empirical orthogonal function (EOF) modes of OLR and wind, and the two modes appear as a quadrature pair that demonstrates a large-scale eastward-propagating intraseasonal signal. In Figure 13 of *Virts and Wallace* [2010], the TTL cirrus cloud signature forms the horseshoe-shaped structure during the phase when the active convection anomaly is centered over the western Pacific.

Previous studies of the variability in the tropical intraseasonal oscillation (ISO) have emphasized the relationship with El Niño–Southern Oscillation (ENSO). A local response of the MJO to ENSO in the Pacific is mostly observed in the southern summer. *Fink and Speth* [1997] and *Hendon et al.* [1999] showed that MJO activity propagates about 20° longitude farther eastward during El Niño periods than during non-El Niño periods by using the variance of band-pass-filtered OLR. A similar result was found by *Gutzler* [1991] by using lower tropospheric zonal wind. *Kessler* [2001] found that the third EOF mode of OLR and zonal wind captures the eastward extension of the MJO envelope during El Niño events.

An example of year-to-year variations of ISO activity unrelated to ENSO has been illustrated by *Hendon et al.* [1999]. They displayed two types of ISO by using the unfiltered tropical OLR data in the southern summer during the weak ENSO periods (Figure 1.12); One type exhibited the character of planetary-scale eastward propagation from the western Indian Ocean to near the date line, and the other the character of quasi-stationary fluctuations at the longitude of the Australian summer monsoon. The active convections of these two ISOs also showed different features of the intensity, location, and duration from each other. *Roundy* [2012a,b,c] have examined the range of propagation speed that is observed in the convective anomaly of the MJO-Kelvin continuum, based on the idea that Kelvin waves and the MJO are not dynamically distinct modes. Various types of the ISO propagation appear in the unfiltered OLR field and they would have different impacts on the temperatures around the tropi-

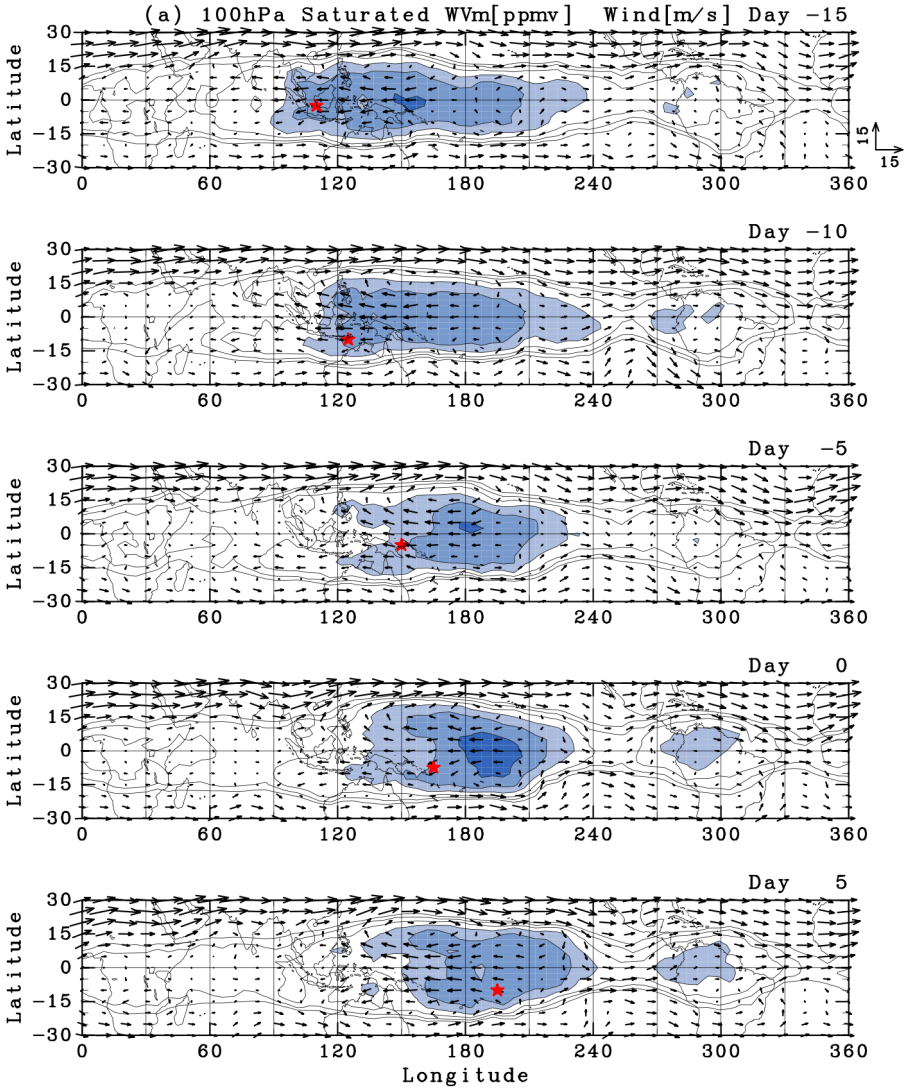


Fig. 1.11 Longitude–latitude sections of saturation mixing ratio from temperature (ppmv, contours and colors) and horizontal wind components ($\mathrm{m\,s^{-1}}$, vectors) at 100 hPa. A red star indicates the convective center on each day. Contour intervals are 1.0 ppmv. Light blue indicates less than 5.0 ppmv. Dark blue indicates less than 3.0 ppmv. From *Eguchi and Shiotani* [2004].

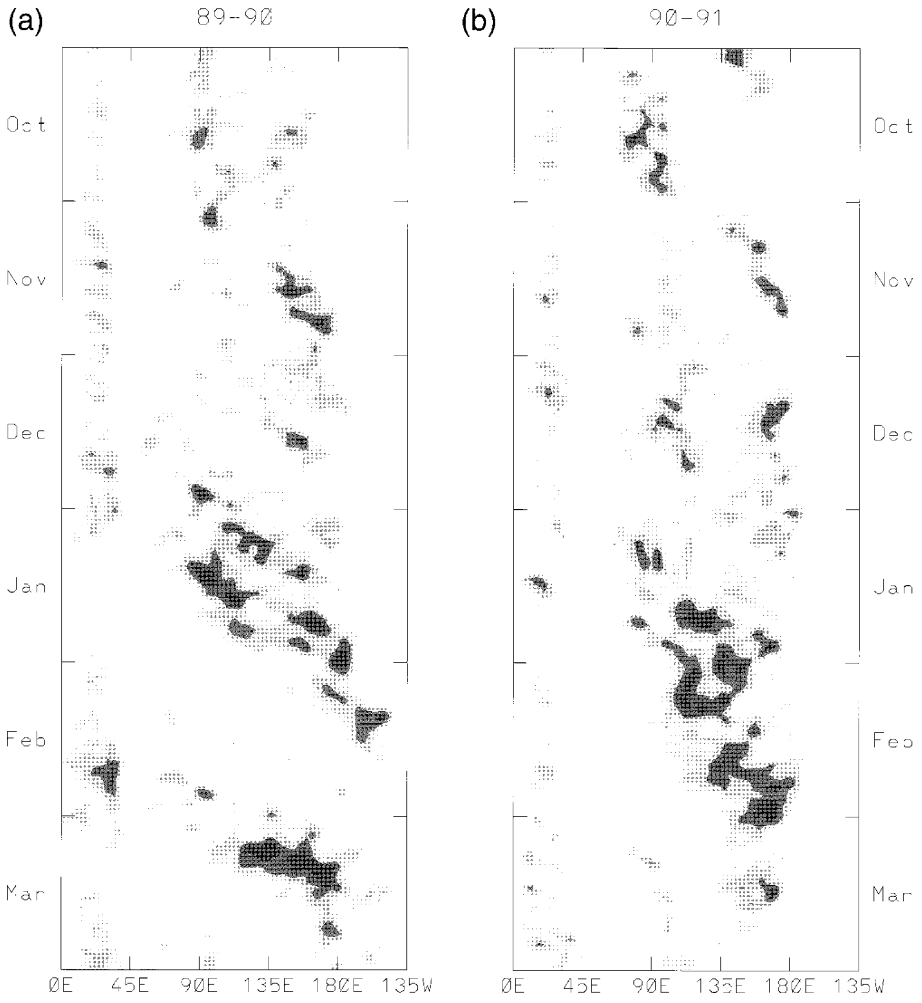


Fig. 1.12 Longitude–time sections of daily OLR (shaded for values less than 225 W m$^{-2}$, shading interval 10 W m$^{-2}$) for (a) Oct 1989–Mar 1990, and (b) Oct 1990–Mar1991. OLR was averaged longitudinally 5°N–10°S and low-pass filtered with one pass of a 1–2–1 running mean. From *Hendon et al.* [1999].

cal tropopause and consequently the dehydration process in the TTL. However, the statistical analysis to distinguish the ISO propagation types has not been adequately assessed yet.

## 1.4 Object of the Thesis

The Tropical Tropopause Layer (TTL) is a region within which air has characteristics of both the troposphere and the stratosphere. The main objective of this thesis is to understand the atmospheric dynamics in the TTL. It has been thought that the atmospheric response around the TTL occurs to the heating generated by the tropical convections in the troposphere, as shown in theoretical model studies. However, observational study to confirm the relationship between them and reveal the response variations which occur as the heating intensity is changed has not been conducted adequately. Main emphasis in this thesis is put on a large-scale spatial structure of the tropical tropopause temperature because temperature around the tropical tropopause is one of the most important factors controlling water vapor mixing ratio in the lower stratosphere.

The structure of the thesis is the follows. In chapter 2, the data sets used in this thesis are described. Chapter 3 presents an analysis of the climatological behavior of the temperature structure, including its seasonal and interannual variability by using the monthly mean data. An index is established to represent tropopause temperatures forming a horseshoe-shaped structure, motivated by the Matsuno–Gill solutions to tropical heating. Statistical analysis of investigating the relationship with convective activities is conducted by using the horseshoe-shaped structure index. The main body of chapter 3 is based on *Nishimoto and Shiotani* [2012a]. Shorter timescale variability such as the intraseasonal oscillations is examined in chapter 4 by using the daily mean data. While chapter 3 focuses on the stationary component, chapter 4 examines the traveling one. Cluster analysis is first performed according to the ISO propagation features of convective activities observed in the daily OLR field. The relationship between the tropopause temperatures and the convective activities is then investigated for each cluster. The main body of chapter 4 is based on *Nishimoto and Shiotani* [2012b]. Finally, chapter 5 concludes this thesis and the findings.

# Chapter 2

# Data

Reanalyses data from the European Centre for Medium-range Weather Forecasts (ECMWF) are used to investigate space and time variations in the tropical atmosphere. In chapter 3, the monthly mean ERA-40 data [*Uppala et al.*, 2005] with a 2.5° grid spatial resolution is used to examine the seasonal and interannual variability. In chapter 4, ERA-Interim data sets [*Dee et al.*, 2011] are used to examine the intraseasonal variability in temperature, wind, and sea surface temperature (SST) fields. The original data are provided at 6 hours intervals with a 1.5° grid spatial resolution, but in this study they are reconstructed with the same time and spatial resolutions as those used in the outgoing longwave radiation (OLR) data, that is, a daily mean with a 2.5° grid spatial resolution. The 100-hPa temperature data are used to investigate variations in the temperature around the tropical tropopause. The temperatures at the 100-hPa level, which is generally located lower than the cold-point and lapse-rate tropopause during the southern summer, are a few degrees higher than the cold-point and lapse-rate tropopause temperatures [*Seidel et al.*, 2001].

As a proxy for convective activities over the tropical region, monthly and daily mean OLR data are obtained from the National Oceanic and Atmospheric Administration (NOAA) satellites [*Gruber and Krueger*, 1984] with a 2.5° grid spatial resolution. In addition, to assess the effect of ENSO on interannual variability in tropical tropopause temperatures, the Southern Oscillation index (SOI) is used as a measure of ENSO

status. The SOI data are obtained from the Climate Prediction Center web site http://www.cpc.ncep.noaa.gov/ and were calculated as the difference between sea level pressures in Tahiti (18°S, 150°W) and Darwin (12°S, 131°E).

# Chapter 3

# Seasonal and Interannual Variability

As seen in Figure 1.3, low temperatures generally occur over the equator and extend northwestward and southwestward in the subtropics to form the horseshoe-shaped structure. The horseshoe-shaped temperature structure resembles the stationary wave response known as the Matsuno–Gill pattern. However, the relationship with tropical convection, which is a possible heating of the horseshoe-shaped structure, is unclear yet. This chapter reveals the seasonal and interannual variability of the horseshoe-shaped temperature structure around the tropical tropopause and its relationship with convective activities over the monsoon regions by using the monthly mean data. The analyses are conducted from January 1979 to August 2002 (end of the ERA-40 data period) because improved satellite irradiance data were assimilated during this period.

General characteristics of the tropical tropopause temperatures are described in section 3.1. Two preliminary indices are first defined in section 3.2, by focusing on the temperature field characteristics of the Matsuno–Gill pattern. In section 3.3, an index characterizing a horseshoe-shaped structure (HSI-1) is derived by combining these two indices. Variability in the horseshoe-shaped structure index and its relationship with convective activities are investigated for seasonal and interannual time scales in sections 3.4 and 3.5, respectively. Finally, section 3.6 summarizes the study.

## 3.1 General Characteristics of Tropical Tropopause Temperatures

The horizontal distribution of monthly mean temperatures at 100 hPa and OLR ($\leq$ 220 W/m$^2$) in August 1995 and February 1984 is shown in Figures 3.1a and 3.1b, respectively. The tropopause temperatures during the northern and southern summers have previously been illustrated by using radiosonde data [*Newell and Gould-Stewart*, 1981] and reanalysis data [*Highwood and Hoskins*, 1998; *Hatsushika and Yamazaki*, 2001]. Tropical temperatures are higher in the northern summer (Figure 3.1a) than in the southern summer (Figure 3.1b), resulting from the annual cycle of tropopause temperatures [*Seidel et al.*, 2001]. The two cases, August 1995 and February 1984, are chosen for the following reasons: 1) They are weak ENSO years, and 2) they are typical examples that show low temperatures extending to the north-west and south-west toward the subtropics to form a horseshoe-shaped structure.

In Figure 3.1a for the northern summer, low temperatures are located in the western Pacific around the equator, in the Arabian Sea and South Asia in the northern subtropics around 15°N, and north of the Australian continent in the southern subtropics around 10°S. These low temperatures form the horseshoe-shaped structure. Consistent with *Nishi et al.* [2010], isolated high temperatures are located around the equator between 45°E and 90°E, surrounded by the horseshoe-shaped temperature structure.

A strong convective area (low OLR) for the northern summer (Figure 3.1a) is located between ~75°E and 150°E in the Northern Hemisphere. *Murakami and Matsumoto* [1994] divided this convective area into two regions on the basis of different mechanisms of development of the two monsoon systems. One is known as the South Asian monsoon (SoAM) region in the Bay of Bengal, and the other is the North Pacific monsoon (NPM) region in the western Pacific. The two centers of the convective areas are located around 90°E and 15°N for the SoAM region and around 135°E and

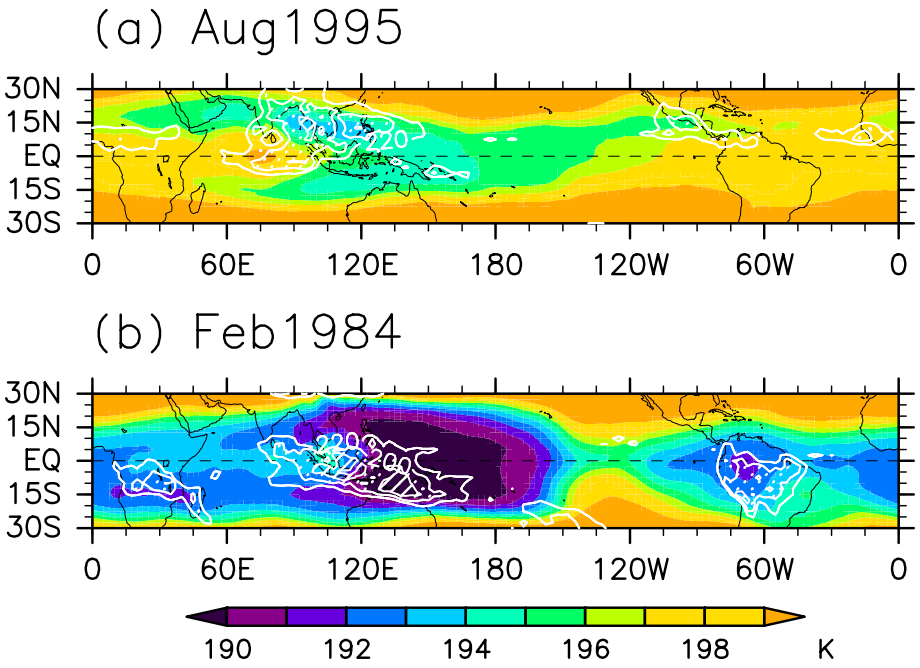


Fig. 3.1 Maps of temperature at 100 hPa (K; color) and OLR ($W/m^2$; white contour) at (a) August 1995 and (b) February 1984. Contours of OLR are drawn only 180, 200 and 220 $W/m^2$.

10°N for the NPM region (Figure 3.1a). This feature is further examined in Figure 3.5, which shows a longitude–time section of the tropical (20°S–20°N) mean OLR.

In Figure 3.1b for the southern summer, low temperatures are located in the western Pacific around the equator and in the northern and southern subtropics around 15°N and 15°S between 90°E and 120°E, forming the horseshoe-shaped structure. Convective activities are present in the Southern Hemisphere in and adjacent to the Australian monsoon (AUM) region between ~90°E and 150°E.

A comparison of temperature and OLR distributions during the Southern Hemisphere monsoon season with those during the Northern Hemisphere monsoon season reveals that the horseshoe-shaped structure during the Northern Hemisphere monsoon season is distributed more widely in the longitude and is accompanied by the two convective areas, as mentioned previously. The horseshoe-shaped structure present

during the southern summer is similar to that observed in a simulation result for the tropopause temperature with a single idealized heating shown by *Highwood and Hoskins* [1998]. Hence, a concept is proposed that the two convective areas during the northern summer result in such a wide distribution of the low temperatures that the horseshoe-shaped structure forms.

## 3.2 Variability in the Horseshoe-shaped Structure

### 3.2.1 Definition of HSI-R and HSI-K

Figure 3.2 shows a schematic illustration of the horseshoe-shaped temperature structure, which resembles a stationary wave response known as the Matsuno–Gill pattern [*Matsuno*, 1966; *Gill*, 1980], which consists of the Rossby response in the western part and the Kelvin response in the eastern part. Therefore, two indices, HSI-R and HSI-K, are first defined as representing longitude–time variations in the Rossby and Kelvin responses, respectively. Then, in section 3.3, the combined index is further defined from these two indices to investigate longitude–time variations in the horseshoe-shaped temperature structure.

As a representative of the Rossby response, the index HSI-R is calculated by a curvature of the 100-hPa temperature along the meridional circle at the equator and is given as a function of longitude $x$ and time $t$:

$$\text{HSI-R}(x,t) = \frac{T_N(x,t) + T_S(x,t)}{2} - T_{Eq}(x,t),$$

where $T_{Eq}(x,t)$ is the temperature at the equator, and $T_N(x,t)$ and $T_S(x,t)$ are temperatures in the subtropics in the Northern and Southern Hemispheres, respectively. The latitude bands for $T_N(x,t)$ and $T_S(x,t)$ are defined as an average between 10°N and 15°N and between 10°S and 15°S, respectively, because it was detected that low temperatures representative of the Rossby response are mostly located around these latitudes by checking the 100-hPa temperature data in every month. When low temperatures occur in the subtropics as the Rossby response, this index becomes

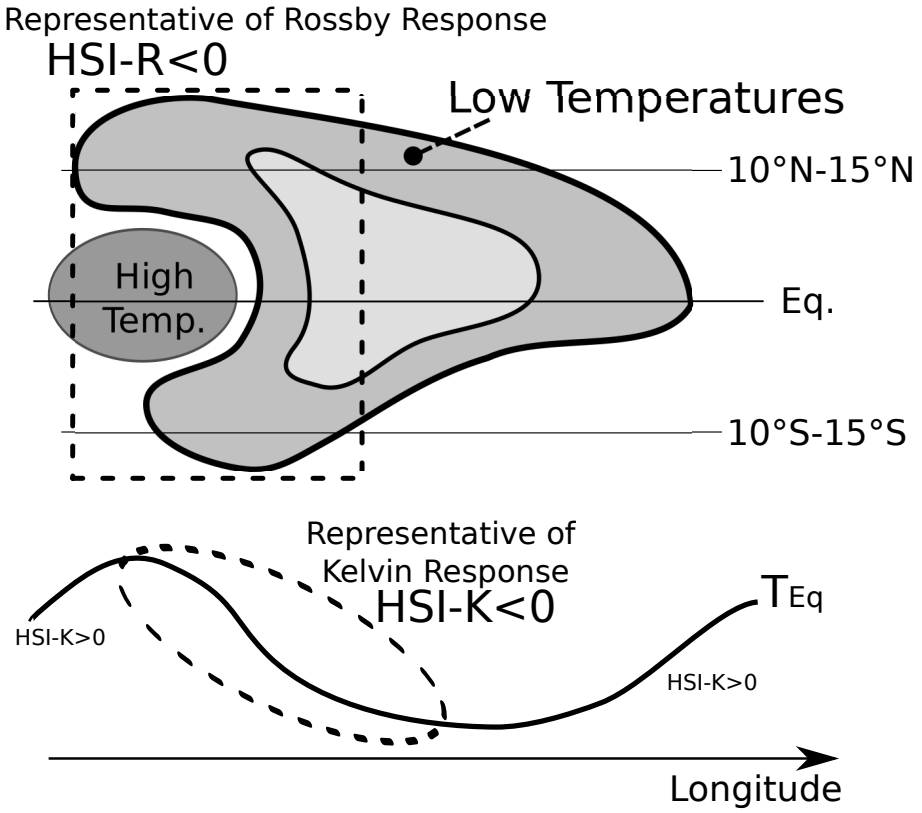


Fig. 3.2 Schematic diagram of the horseshoe-shaped structure and an explanation of HSI-R and HSI-K.

negative.

As a representative of the Kelvin response, the index HSI-K is calculated by a zonal gradient of the 100 hPa temperature along the equator and is given as a function of longitude $x$ and time $t$:

$$\text{HSI-K}(x,t) = T_{Eq}(x + \Delta x/2, t) - T_{Eq}(x - \Delta x/2, t).$$

When the temperature structure represents of the Kelvin response, this index becomes negative. A differentiation length, $\Delta x$, is set at 20° longitude. A visual inspection of Figure 3.1 indicates that this length is sufficiently large to detect the Kelvin response and to eliminate effects of small-scale features.

In the horseshoe-shaped structure, negative values of HSI-K are located slightly to

the east of the negative values of HSI-R (Figure 3.2), which is in agreement with the Matsuno–Gill pattern [*Matsuno*, 1966; *Gill*, 1980]. In addition, the two indices may change accordingly with a positive correlation in response to heating generated by convective activities in and adjacent to monsoon areas.

### 3.2.2 Climatological Features

Figures 3.3, 3.4, and 3.5 show longitude–time sections of the HSI-R, HSI-K, and OLR averaged over 23 years during 1979–2002 for each month, respectively, revealing their climatological features. OLR values are averaged between 20°S and 20°N to include the monsoon regions located in the subtropics (Figure 3.1).

In general, values of both HSI-R and HSI-K are negative and those of OLR are low in the Eastern Hemisphere. These values show similar clear seasonal cycles of strong negative (low) values during the northern and southern summers. As expected from the definition of the two indices mentioned in section 3.2.1, negative HSI-K peaks are located east of negative HSI-R peaks. Hence, the horseshoe-shaped structure frequently appears in the Eastern Hemisphere during the northern and southern summers. The longitudinal phase relationship between HSI-R and HSI-K is surveyed in detail in section 3.2.3.

In the Western Hemisphere, where values of HSI-R are always positive, two maxima of HSI-R occur from November to May: one is located between 160°W and 75°W, and the other is between 45°W and 0°W. At the western and eastern sides of the two HSI-R maxima, values of HSI-K are positive and negative, respectively. This feature in the Western Hemisphere corresponds to the narrow latitudinal extents of the cold tropical tropopause around 120°W and 30°W (Figure 3.1b).

Regarding the horseshoe-shaped structure, the negative HSI-R values in the Eastern Hemisphere (Figure 3.3) are strong in two seasons, as previously mentioned. One occurs during the northern summer from June to October over a large area between 30°E and 150°E, and the other occurs during the southern summer from December to March over a narrow area between 90°E and 120°E; the former is much stronger than

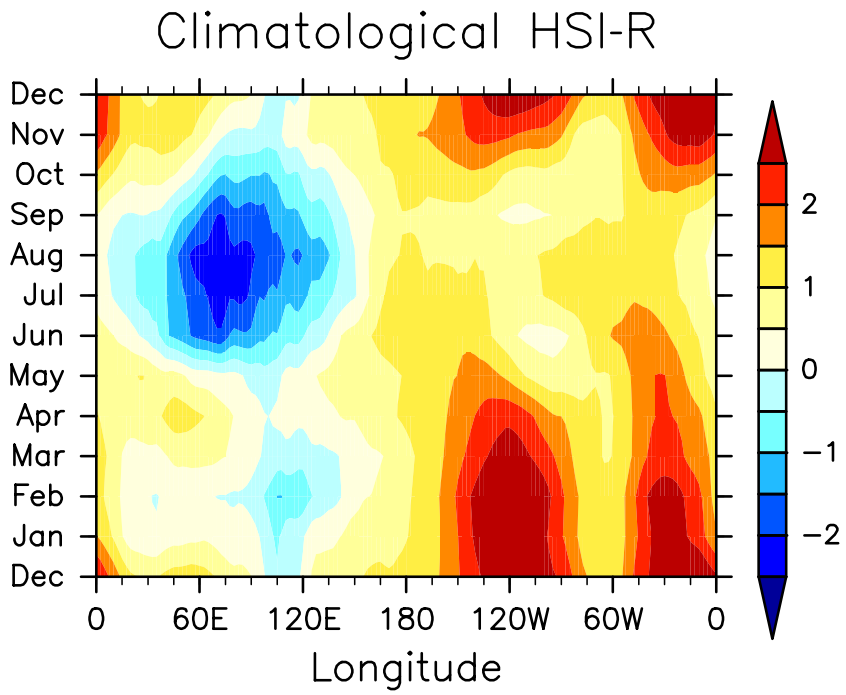


Fig. 3.3 Longitude–time section of HSI-R, which represents the Rossby response, averaged over 23 years (1979–2002) at each month.

the latter. As detailed in Figure 3.5, the two monsoon regions with low OLR present in the Eastern Hemisphere during the northern summer are distinctly separated around 120°E. Correspondingly, two peaks occur in the negative HSI-R values during the northern summer. The stronger peak is at 70°E in August, at which time and place the isolated warm anomaly on the equator is located (Figure 3.1a). The weaker peak is at 120°E in August. During the southern summer, a weaker negative peak occurs in HSI-R around 105°E in February rather than that during the northern summer.

In Figure 3.4, strong negative HSI-K values occur in the Eastern Hemisphere for two seasons. They are similar to those in negative HSI-R values shown in Figure 3.3. One strong negative values occur during the northern summer from May to September and is situated over a wide area between 60°E and 180°E. Similar to that exhibited by HSI-R and OLR in Figures 3.3 and 3.5, respectively, two peaks appear in the longitude. The western peak is stronger and is located around 85°E in July, at

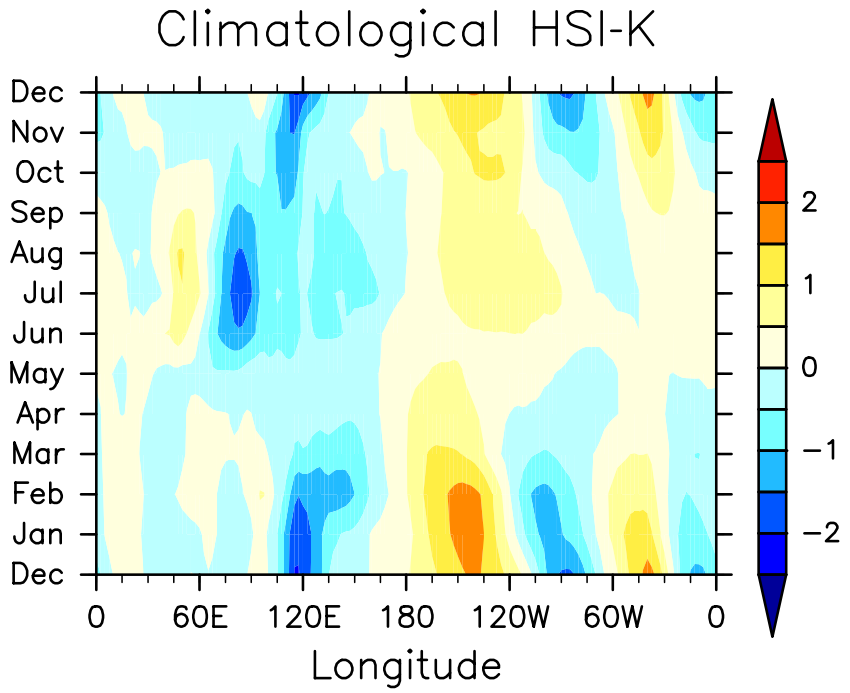


Fig. 3.4 Same as Figure 3.3, but for HSI-K, which represents the Kelvin response.

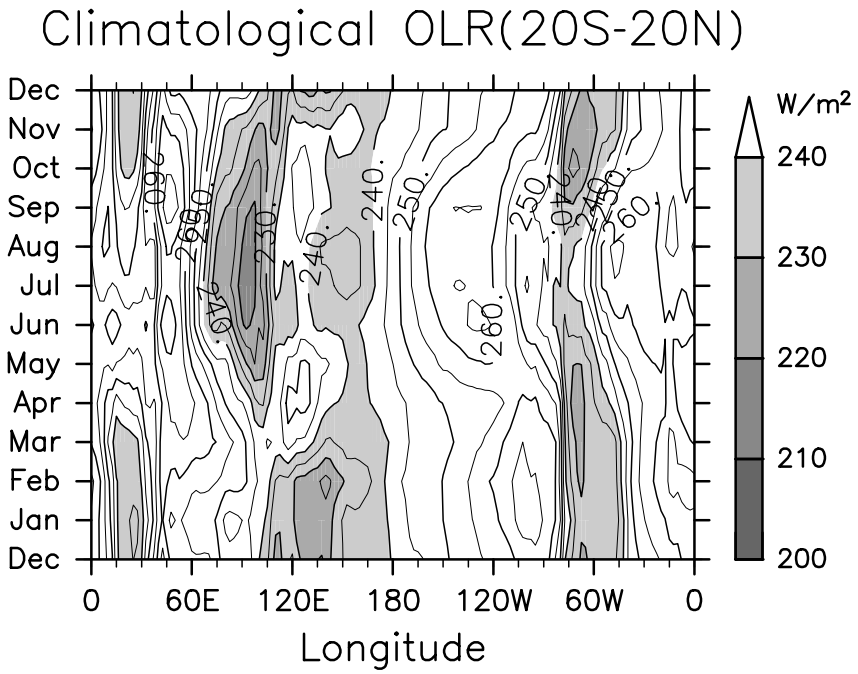


Fig. 3.5 Same as Figure 3.3, but for the tropical (20°S–20°N) mean OLR.

which time and place the eastern edges of the isolated warm anomaly on the equator appear, and the eastern peak is around 145°E in August. The other strong negative value occurs during the southern summer from November to March and is located over a narrow area between 100°E and 150°E, and its peak is located around 120°E in December.

Figure 3.5 shows active convective areas with low OLR between 60°E and 180°E during the northern and southern summers, at which time and place strong negative values occur in HSI-R and HSI-K (Figures 3.3 and 3.4, respectively). These convective activities are expected to be located in and adjacent to the monsoon areas in the Northern Hemisphere during the northern summer and in the Southern Hemisphere during the southern summer. During the northern summer from May to October, low OLR values are divided by the boundary around 120°E, as shown in Figure 3.1a. The western side is located in and adjacent to the SoAM region, with its peak around 90°E in July, and the eastern side is in and adjacent to the NPM region, with its peak around 150°E in August. During the southern summer from December to February, low OLR values are located between 105°E and 150°E in and adjacent to the AUM region with its peak around 140°E in February. These results agree well with *Murakami and Matsumoto's* [1994] previous study on convective activities over these three monsoon areas. The relationship between the horseshoe-shaped structure and convective activities in the monsoon domains is surveyed in section 3.4.

### 3.2.3 Longitudinal Phase Lag between Two Indices

As expected from the definition of the two indices stated in section 3.2.1, the negative HSI-K peaks should be located to the east of the negative HSI-R peaks. The longitudinal phase lag $\alpha$ is examined in Figure 3.6 through calculation of the correlation coefficients between the monthly mean values of HSI-R$(x,t)$ and HSI-K$(x+\alpha,t)$ in the Eastern Hemisphere ($0° \leq x < 180°$), where they are mostly negative (Figures 3.3 and 3.4). The longitudinal phase lag that provides the most significant correlation differs somewhat in the four seasons and is smaller in the southern summer

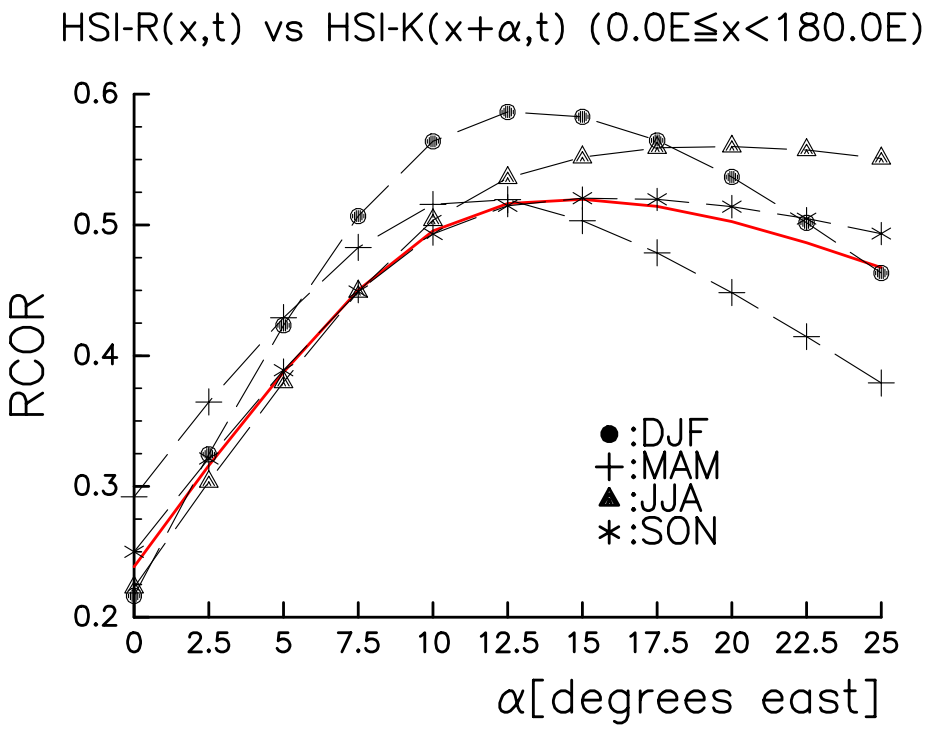


Fig. 3.6 Correlation coefficients between HSI-R and HSI-K in the Eastern Hemisphere with longitudinal phase lag $\alpha$ for HSI-K relative to HSI-R. Black lines and marks show correlation coefficients calculated using the values in each season, and a red line for all season. The legend of marks are shown in a panel.

than in the northern summer (Figure 3.6). This result could be explained by the concept that the horseshoe-shaped structure during the northern summer is zonally more elongated than that during the southern summer because the convective area during the former is zonally more extended than that during the latter (Figure 3.1). The correlation coefficient for all months is most significant ($r = 0.52$) when the phase lag is $+15.0°$ and the correlation coefficient for each season is around 0.5–0.6. Therefore, the longitudinal phase lag of HSI-K relative to HSI-R is set at $+15.0°$ in the following analysis.

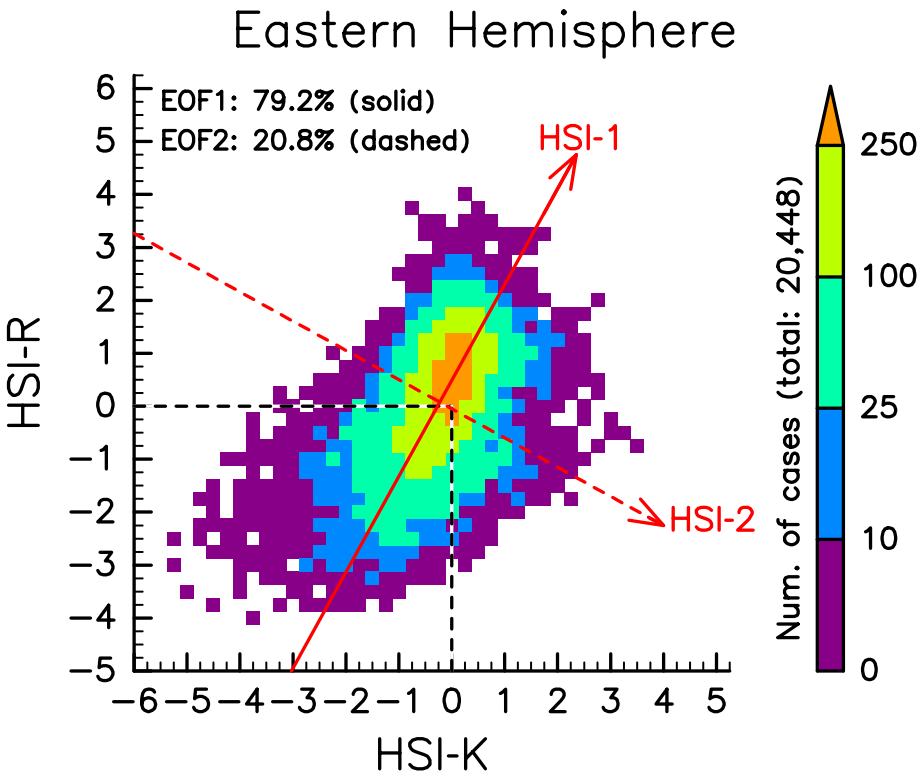


Fig. 3.7 Frequency of occurrence for HSI-K and HSI-R bi-intervals between January 1979 and August 2002 in the Eastern Hemisphere. Red line indicates the linear regression line of the first EOF mode (solid) and the second EOF mode (dashed), which are calculated by using the values in the Eastern Hemisphere.

## 3.3 Combined Index

In this section, the index is defined representing the horseshoe-shaped temperature structure using HSI-R and HSI-K values in the Eastern Hemisphere. Figures 3.7 shows a frequency distribution of the monthly mean values of HSI-R and HSI-K in the Eastern Hemisphere from January 1979 to August 2002. Here the longitudinal phase lag is set +15.0° for HSI-K relative to HSI-R. An empirical orthogonal function (EOF) analysis is performed with the covariance matrix of HSI-R and HSI-

K in the Eastern Hemisphere. The red solid line in Figure 3.7 represents the first basis function, hereafter termed HSI-1$(x,t)$, accounting for 79.2% of the total variance; HSI-1$(x,t) = 1.12 \times$ HSI-R$(x,t) + 0.618 \times$ HSI-K$(x+15°,t)$. Therefore, when the HSI-1 value is negative, the temperature field should be representative of the horseshoe-shaped structure. The second basis function, hereafter termed HSI-2$(x,t)$, is indicated in Figure 3.7 as a red dashed line, accounting for 20.8% of the total variance; HSI-2$(x,t) = -0.317 \times$ HSI-R$(x,t) + 0.57 \times$ HSI-K$(x+15°,t)$.

## 3.4 Seasonal Variability in Monsoon Regions

Figure 3.8 shows longitude–time sections similar to that indicated in Figure 3.3, but for HSI-1 and HSI-2 in the Eastern Hemisphere. The seasonal variation in HSI-1 value (Figure 3.8a) is almost identical to that in the climatological HSI-R and HSI-K values in the Eastern Hemisphere (Figures 3.3 and 3.4, respectively). Negative HSI-1 values are strong during the northern summer between 45°E and 150°E and are distinctly separated by the boundary around 110°E. The western area peaks in July at 70°E, where the isolated warm anomaly on the equator appears. The eastern area peaks around 120°E in August. During the southern summer between 90°E and 120 °E, a strong negative HSI-1 area occurs with a peak around 105°E in February.

The seasonality of the negative HSI-1 also shows a good correspondence to that of the climatological OLR values in the SoAM, NPM, and AUM regions (Figure 3.5), which are located about 10°–20° degrees east of the negative HSI-1 values. Figure 3.9 shows scatterplots of the OLR and HSI-1 values averaged over 23 years for each month over the (a) SoAM, (b) NPM, and (c) AUM domains, which are selected as summarized in Table 3.1. Strong positive correlations between the OLR and HSI-1 values occur during May–December in the SoAM and NPM domains and during November–April in the AUM domain. Hence, the seasonal cycle in the horseshoe-shaped structure is clearly related to convective activities over the three monsoon domains.

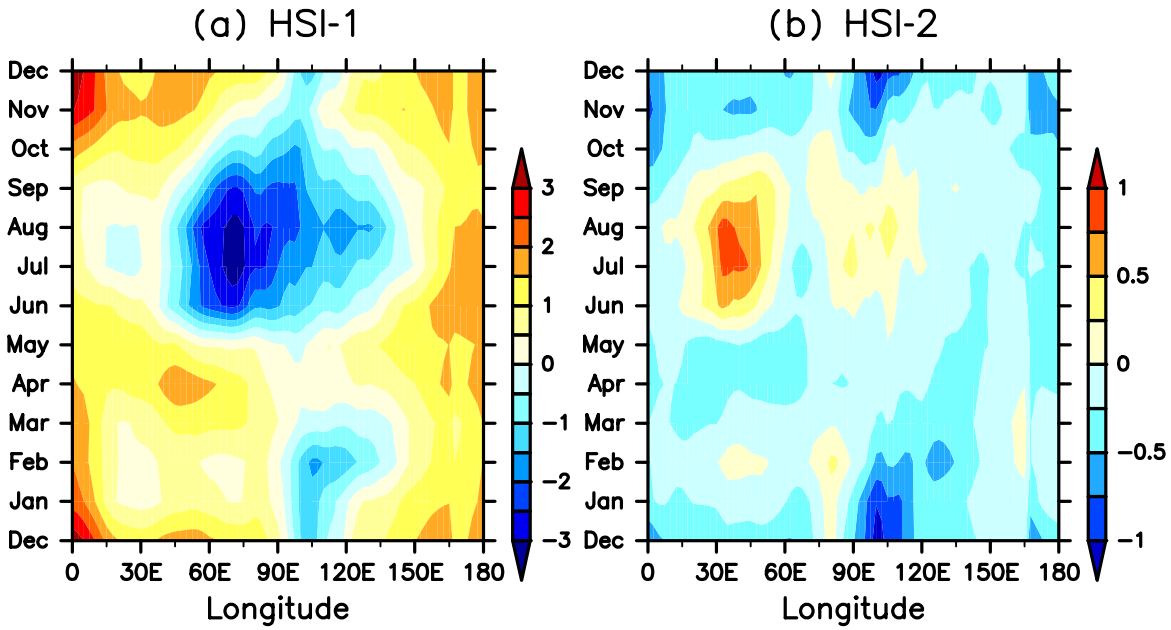


Fig. 3.8 Same as Figure 3.3, but for (a) HSI-1 and (b) HSI-2 in the Eastern Hemisphere.

Table. 3.1 The domains of HSI-1 and OLR for SoAM, NPM, and AUM.

| | SoAM | NPM | AUM |
|---|---|---|---|
| HSI-1 | 60°E–90°E | 110°E–150°E | 100°E–120°E |
| OLR | 5°N–20°N | 5°N–20°N | 15°S–10°N |
| | 70°E–110°E | 130°E–180°E | 110°E–150°E |

As shown in Figure 3.8b, HSI-2 values are positive west of the negative HSI-1 peaks, with the most extreme located over 30°E–60°E during June–September. This result could refer to the western edges of the isolated high temperatures at the equator, which are surrounded by temperatures with the horseshoe-shaped structure, because an HSI-2 value can be positive when an HSI-R value is negative and an HSI-K value is positive (Figure 3.7). In fact, the climatological HSI-R and HSI-K values over 30°E–60°E during the northern summer are negative and positive, respectively (Figures 3.3 and 3.4).

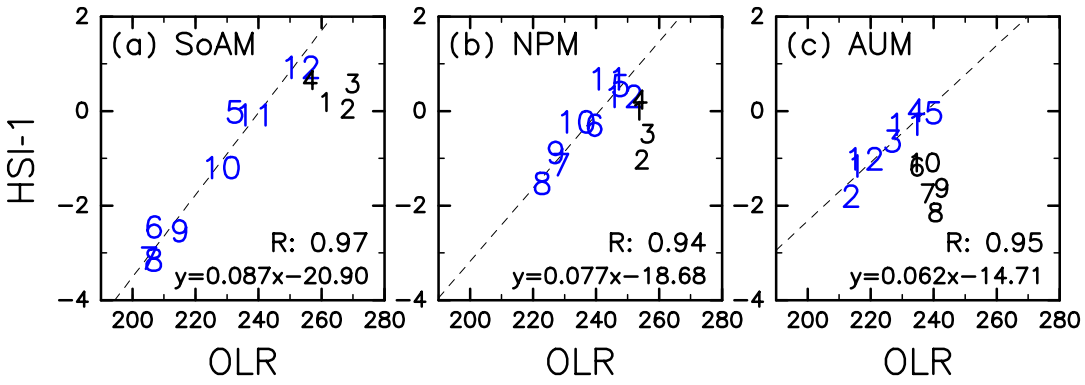


Fig. 3.9 Scatterplots of the climatological OLR and HSI-1 values in the (a) SoAM, (b) NPM, and (c) AUM domains. The number on the scatterplots refers to the month of the data. Correlations and regression lines (indicated by dashed lines) are calculated by using data during May–December in the SoAM and NPM domains and during November–April in the AUM domain.

## 3.5 Interannual Variability and its Link to ENSO

In the previous section, it was shown that the seasonal variation in HSI-1 for each of the three monsoon regions is clearly related to the corresponding convective activities indicated by the OLR values. In this section, interannual variation in HSI-1 is examined such as that due to the ENSO cycle. The ENSO effect is expected to be maximum during the southern summer, involving migration of convective activities over the Pacific [e.g., *Yulaeva and Wallace*, 1994; *Gettelman et al.*, 2001]. On the other hand, during the northern summer, strong convective activities in and adjacent to the monsoon regions are robust features, therefore, ENSO may not necessarily directly affect interannual variation in convective activity and HSI-1. In the following section, the cases are first investigated during the northern summer for the SoAM and NPM domains, then during southern summer when the AUM domain is highly affected. For the latter analysis, to capture the migration in association with ENSO, our analysis is extended in the longitudinally-moving frame of HSI-1 and OLR.

### 3.5.1 Northern Summer

Figure 3.10 shows scatterplots of OLR and HSI-1 values averaged over the (a) SoAM and (b) NPM domains over July–August for each year. In these two months, the climatological HSI-1 in each of the monsoon domains reaches its negative peak (Figures 3.9a and 3.9b). The correlation coefficient is significant in the NPM domain, suggesting that the HSI-1 value is affected by convective activities even in the interannual time scale, but not in the SoAM domain.

*Kawamura et al.* [2001b] showed that in the NPM area, interannual variation in convective activity is related to the ENSO signal in the previous winter via the response of sea surface temperatures over the Indian Ocean. In fact, the lag correlation coefficient between the OLR values averaged over July–August in the NPM domain and the SOI values averaged over January–February in the same year is $-0.54$, higher than the simultaneous correlation coefficient of 0.24 (neither shown). Hence, the lag correlation coefficient between the HSI-1 values in the NPM domain and the SOI values in the previous winter is significant ($-0.49$) (Figure 3.11b).

In the SoAM domain, although the relationship with convective activities is not evident (Figure 3.10a), the simultaneous correlation coefficient between SOI and HSI-1 values (Figure 3.11a) is significant. To examine the interannual variability in the SoAM domain in detail, distributions of temperature at 100 hPa and OLR during July–August are composed for two cases. The first (Figure 3.12a) is for a "strong" case reflecting a strongly negative HSI-1 value in the SoAM domain (1988 and 1991); the second (Figure 3.12b) is for a "weak" case reflecting an HSI-1 value of nearly zero (1982, 1987, 2001, and 2002). Because the strong and weak cases are comparable with the La Niña and El Niño years, respectively, the lowest temperature area at the equator is located over the western Pacific for the strong case and shifts eastward around 160°W for the weak case, which is in agreement with the composite difference between the El Niño and La Niña years during the northern summer presented by *Hatsushika and Yamazaki* [2001]. It is detected that strong negative HSI-1 values in

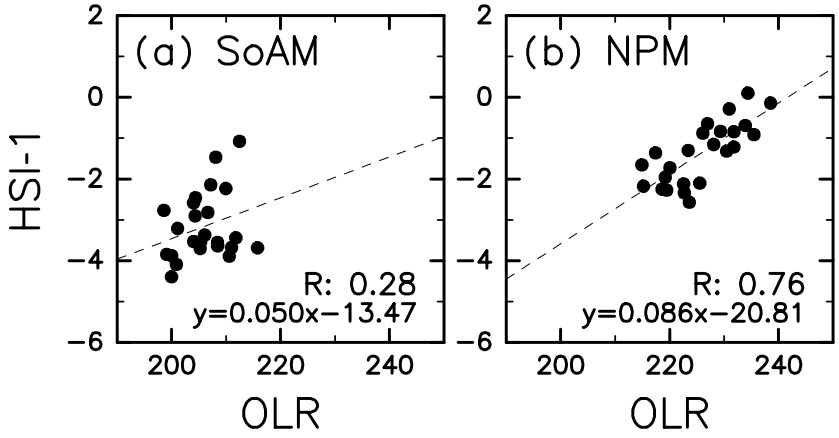


Fig. 3.10 Scatterplots of OLR and HSI-1 values averaged over July–August in the (a) SoAM and (b) NPM domains. Dashed lines indicate linear regression lines.

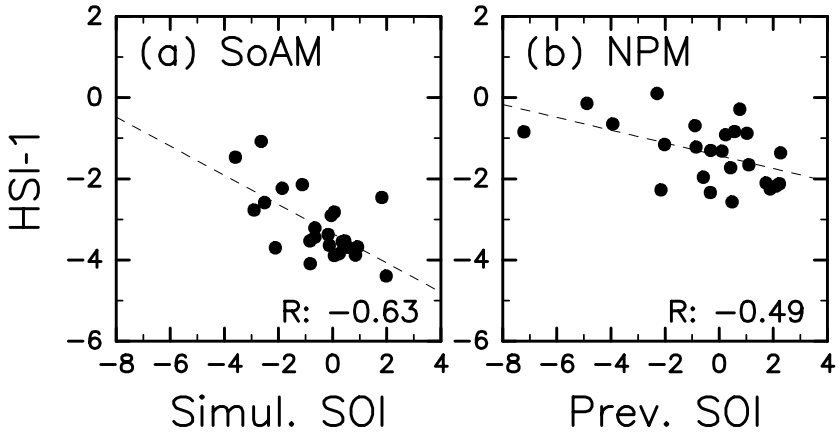


Fig. 3.11 Same as Figure 3.10, but for (a) SOI values in simultaneous season and HSI-1 values in the SoAM domain and for (b) SOI values in previous winter and HSI-1 values in the NPM domain.

the SoAM domain during July–August indicate prominent warm anomalies around 60°E surrounded by the horseshoe-shaped temperature structure.

*Nishi et al.* [2010] reported that strength in the warm anomalies is weak in the strong El Niño years, which agrees with our results, although they did not show the relationship with convective activities. In addition, the researchers suggested

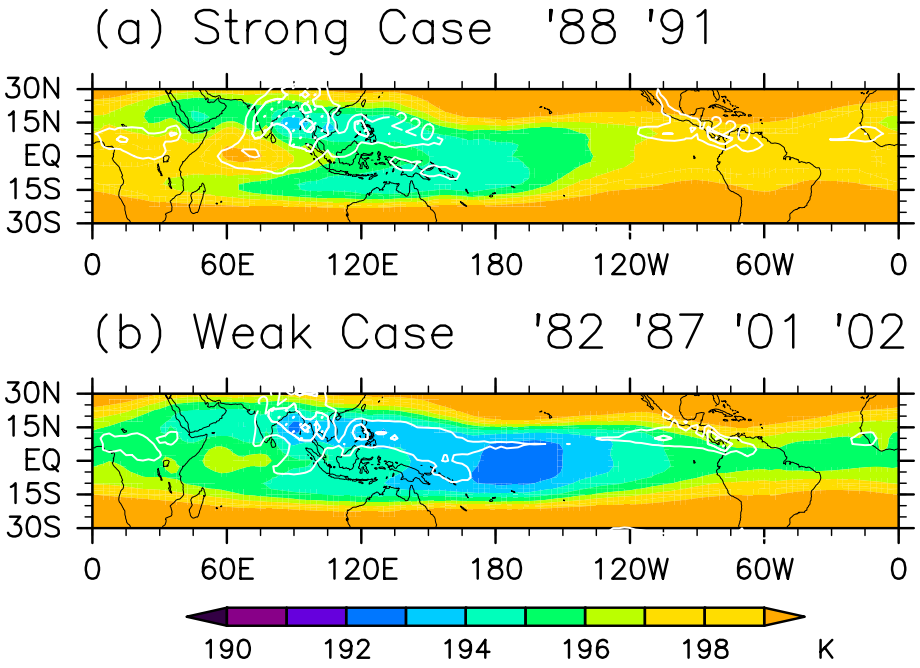


Fig. 3.12 Composite maps of temperature at 100 hPa (K; color) and OLR ($W/m^2$; white contour) for (a) the strong case reflecting a strongly negative HSI-1 value in the SoAM area, and (b) the weak case reflecting an HSI-1 value of nearly zero. OLR contours is drawn only 200 and 220 $W/m^2$.

that tropical easterly winds, which are part of an anticyclonic circulation over the Tibetan Plateau in the upper troposphere and the lower stratosphere, can relate to the intensity of the warm anomalies. The anticyclone could be maintained by sensible heating over the Tibetan Plateau, and the intensity of the anticyclone varies with the life cycle of ENSO [*Hoskins and Wang*, 2006]. However, the mechanism of formation and variability of the warm anomaly remains to be discussed.

### 3.5.2 Southern Summer

A correlation coefficient between OLR and HSI-1 values averaged over the AUM domain (i.e., the longitudinally-fixed frame) over January–February for each year is significant at 0.83 (not shown). However, convective activities over the Pacific migrate

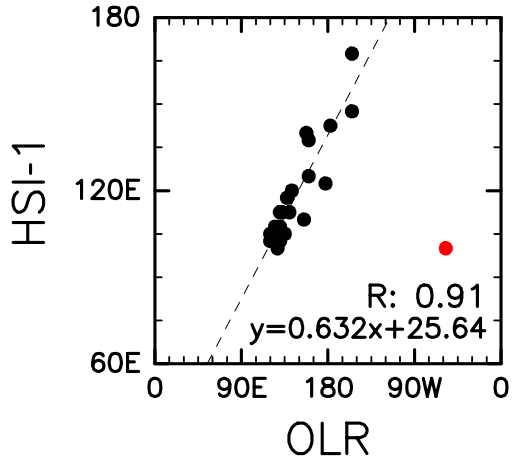


Fig. 3.13 Scatterplot of longitudes of OLR and HSI-1 minima in each year during January–February. A red dot refers to the 1990 case. Correlation and regression line (indicated by dashed lines) are calculated using the values excluding the 1990 case.

with the ENSO cycle during the southern summer [e.g., *Yulaeva and Wallace*, 1994; *Gettelman et al.*, 2001]; therefore, the relationship between OLR and HSI-1 values in the longitudinally-moving frame is examined further.

Figure 3.13 shows the relationship between longitudes of OLR and HSI-1 minima in each year. These OLR and HSI-1 values are averaged over January–February, and the OLR values are further averaged over 15°S–10°N and smoothed by a running mean for 42.5° longitude. It is detected that the HSI-1 minima are located around 100°E–120°E in most years, accompanied by OLR minima around 110°E–150°E; these regions correspond to the AUM area as summarized in Table 3.1. In some years, the HSI-1 minima move to the east of 135°E; these years are basically in the El Niño phase. The longitudinal phase difference between HSI-1 and OLR is larger as the minima shift eastward. This relation is significant with a correlation coefficient of 0.91, except for the case in January–February 1990, marked by a red dot. *Hayes et al.* [1991] and *Bergman et al.* [2001] reported that although early stages of El Niño development were evident in February 1990, El Niño did not develop fully after that

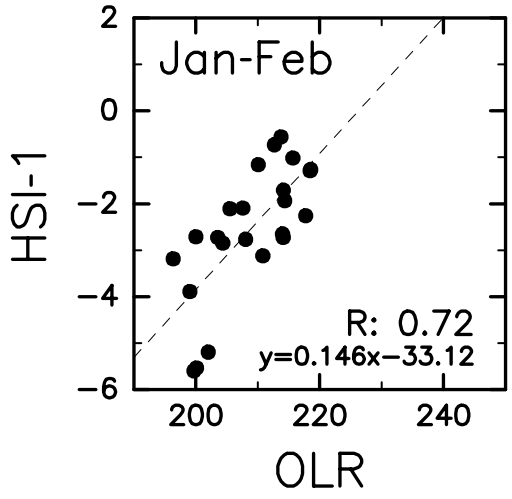


Fig. 3.14 Same as Figure 3.10, but for OLR and HSI-1 minima in the longitudinally-moving frame during January–February. The 1990 case is omitted.

time. Figure 3.14 reveals a positive correlation between the OLR and HSI-1 minima in the longitudinally-moving frame; the case in January–February 1990 is omitted.

Figure 3.15 displays composite maps for the strong and weak cases, similar to that shown in Figure 3.12. In Figure 3.15a, the strong case represents years when the HSI-1 minimum in the moving frame during January–February is strongly negative (1984, 1996, and 2000), and Figure 3.15b shows the weak case representing years at nearly zero (1983, 1988, and 1993). Because those years for the strong and weak cases are in La Niña and El Niño phases, respectively, the following features in the composites are consistent with those for the El Niño and La Niña years in both the tropopause temperature [*Hatsushika and Yamazaki*, 2001] and convective activities [*Yulaeva and Wallace*, 1994; *Gettelman et al.*, 2001]. For the strong case (Figure 3.15a), low temperatures form the horseshoe-shaped structure over the western Pacific, surrounding warm anomalies on the equator around 110°E, and strong convective activities occur over the Australian monsoon region. For the weak case (Figure 3.15b), the low temperature region shifts eastward, and its shape becomes zonally elongated and meridionally narrow, similar to that observed in convective activities.

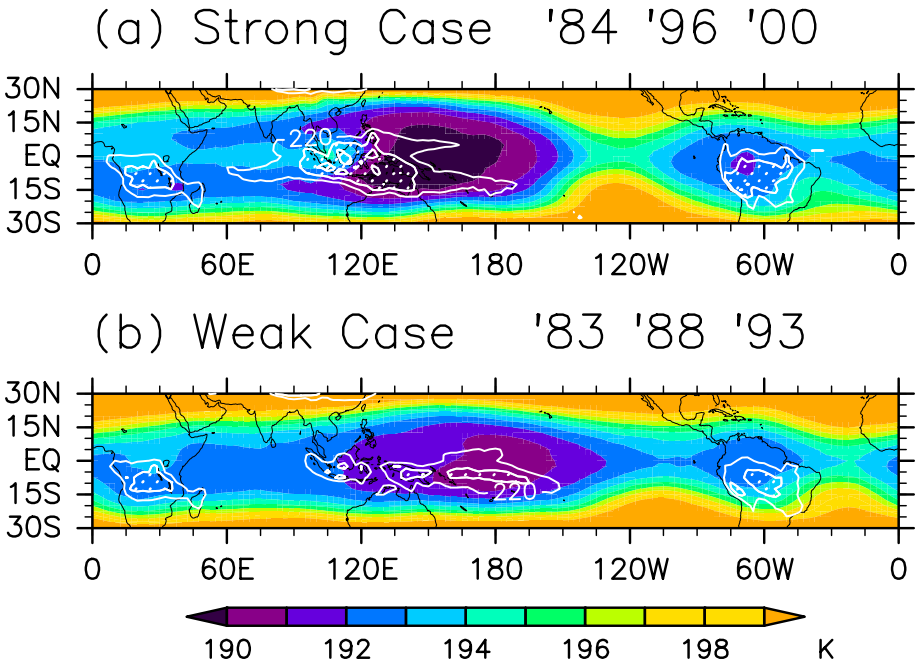


Fig. 3.15 Same as Figure 3.12, but for (a) the strong case in the longitudinally-moving frame during January–February, and (b) the weak case.

### 3.5.3 Variation in Minimum Temperature

The composite temperature fields for the two cases as shown in Figures 3.12 and 3.15 reveals that minimum tropopause temperatures over 15°N–15°S do not differ significantly between the strong and weak cases. For the northern summer, these temperatures are 194.8 K and 193.2 K in the SoAM domain and 194.0 K and 194.1 K in the NPM domain; the respective southern summer temperatures are 189.4 K and 190.6 K. These results agree with previous studies that surveyed the effect of ENSO on a dehydration process [*Gettelman et al.*, 2001; *Fueglistaler and Haynes*, 2005]. However, *Gettelman et al.* [2001] used a water vapor mixing ratio measured from the Halogen Occultation Experiment (HALOE) and concluded the following factors. Strong El Niño conditions (in this study, the weak case for the northern summer in the SoAM domain and for the southern summer) have a moistening impact on the

water vapor mixing ratio of air entering the stratosphere, while La Niña conditions (in this study, the strong case for the northern summer in the SoAM domain and for the southern summer) have a drying impact. Their results agree with AGCM simulations reported by *Hatsushika and Yamazaki* [2003] and *Scaife et al.* [2003] and with the Lagrangian calculations of troposphere-to-stratosphere transport based on ERA-40 temperatures reported by *Fueglistaler and Haynes* [2005]. As *Holton and Gettelman* [2001] and *Hatsushika and Yamazaki* [2003] showed the importance of the horizontal wind circulation in the dehydration process, this discrepancy would account for the strength in the atmospheric circulation accompanied by the horseshoe-shaped structure such as that expressed by the HSI-1 values.

## 3.6 Summary

An index representing a zonally asymmetric temperature structure in the tropical tropopause has been established, and then its variability associated with convective activity has been investigated using ERA-40 and NOAA/OLR data. Particularly during the northern and southern summers, low temperatures persist over the tropics and extend north-west and south-west. These low temperatures form a horseshoe-shaped structure that resembles the Matsuno–Gill pattern, which consists of the Rossby response in the western part and the Kelvin response in the eastern part.

Regarding the horseshoe-shaped structure, two preliminary indices were defined. As a representative of the Rossby response, an index HSI-R$(x,t)$ was calculated from a curvature of the 100-hPa temperature along the meridional circle at the equator; as a representative of the Kelvin response, an additional index HSI-K$(x,t)$ was calculated from a zonal gradient of the 100 hPa temperature along the equator. The two indices were then combined into one index HSI-1 as a result of the EOF analysis using HSI-R and HSI-K values. The index HSI-1 projected a positive linear relation between HSI-R and HSI-K; hence, its negative value should suggest clear existence of the horseshoe-shaped temperature structure.

The negative value of HSI-1 is frequently observed in the Eastern Hemisphere, and its seasonal cycle is closely related to convective activities in and adjacent to the monsoon areas, including the SoAM and NPM domains during the northern summer and the AUM domain during the southern summer. Convective activities in the SoAM and NPM domains may induce two horseshoe-shaped structures individually, and a superposition of the two structures can produce a longitudinally elongated horseshoe-shaped structure during the northern summer.

The ENSO cycle is shown to greatly affect variations in HSI-1 values and convective activities, particularly during the southern summer. As discussed in previous studies [*Yulaeva and Wallace*, 1994; *Hatsushika and Yamazaki*, 2001; *Gettelman et al.*, 2001], low temperatures form the horseshoe-shaped structure over the equator in the western Pacific during the southern summer for the non-El Niño years, while low temperatures shift eastward and becomes more zonally elongated and meridionally narrow for the El Niño years. The longitudinal phase difference between the OLR and HSI-1 minima in the El Niño years is larger than that observed in the non-El Niño years.

During the northern summer, the interannual variability in HSI-1 in the NPM domain is affected by the ENSO cycle in the previous winter, which is consistent with a previous study on convective activities in the NPM area [*Kawamura et al.*, 2001b]. In the SoAM domain, interannual variation in HSI-1 values is not significantly related to convective activities in the monsoon domain. It was detected that the HSI-1 value in the SoAM domain is mainly controlled by the isolated high temperatures observed around 60°E over the equator during July–August, which are surrounded by the horseshoe-shaped structure. The interannual variation in the HSI-1 values is related to the ENSO cycle, which agrees with a previous study on the isolated high temperatures reported by *Nishi et al.* [2010]. The variation in the high temperature may be related to an anticyclone in the upper troposphere over the Tibetan Plateau. However, further discussion is necessary on the detailed mechanism of formation and variability of the isolated high temperatures.

This study clearly revealed the seasonal and interannual variability of the temper-

ature structure around the tropical tropopause and its relationship with convective activities over the monsoon regions with respect to the horseshoe-shaped temperature structure. Relations to shorter time scale oscillations such as intraseasonal oscillation, traveling Kelvin waves and active/break cycles in the Asian monsoon circulation are interesting topics for further investigation. Moreover, numerical experiments are required to validate the use of the index representing the horseshoe-shaped temperature field with respect to convective activities.

# Chapter 4

# Intraseasonal Variability

This chapter reveals the intraseasonal variability in the convective activities and the tropical tropopause temperatures by employing cluster analysis according to the propagation features of the convective centers observed in the daily OLR field. Because the main emphasis here is on coherent eastward-propagating convection that occurs predominantly during the southern summer [e.g., *Hendon et al.*, 1999; *Zhang*, 2005], the analysis is restricted to the southern summer season. 32 complete southern summer seasons are used from January 1979 to December 2011. The OLR data are averaged between 5°N and 15°S, where the convective component of the intraseasonal oscillation (ISO) is most active in the southern summer [e.g., *Hendon et al.*, 1999].

A case study of ISO variations in the convective activity and tropical tropopause temperature during the 1984/85 southern summer, which was during a weak ENSO period, is first presented in section 4.1. The selection of ISO events and the cluster analysis are then documented in section 4.2. Section 4.3 shows the ISO characteristics in each of the clusters, such as convective activity, the horseshoe-shaped temperature structure, tropical tropopause temperatures, and sea surface temperatures (SST). Finally, section 4.4 summarizes the study.

## 4.1 Case Study of the 1984/85 Southern Summer

Figure 4.1 illustrates a longitude-time section of the daily (unfiltered) OLR averaged between 5°N and 15°S for November–March 1984/85. This year is at the weak ENSO period. Two ISO events are detected propagating from the Indian Ocean to the Pacific during this period (the method of selecting ISO events will be described in section 4.2.1): the first one during the middle of November through December and the second one during February through the beginning of March. These two events have different propagation features in the unfiltered OLR field; the second one propagates much faster and farther than the first one while having the stronger active convection of longer duration than the first one. Cluster analysis will be performed according to the ISO propagation features of the active convection observed in the unfiltered OLR field in the next section. The above two events will be grouped into Clusters 3 and 4, respectively.

Figure 4.2 shows the 100-hPa temperature variations associated with the eastward-propagating convection of the second ISO event (February through the beginning of March in 1985). The active convection propagates from the Indian Ocean to near the date line, and accompanies low temperatures to the east around the equator and to the west around 10°N and 10°S. These low temperatures form the horseshoe-shaped structure, which resembles a super position of the Rossby and Kelvin responses and is known as the Matsuno–Gill pattern. Similar low temperatures were observed by *Eguchi and Shiotani* [2004] who created composites of the 100-hPa temperature relative to the passage of five different MJO-related convective systems.

Low temperatures exist over both equatorial South America and Africa in Figure 4.2. The low temperatures appear over South America on 9 February and 1 March and over Africa on 19 February and 1 March, and are more narrowly confined to the equatorial belt than those over the western Pacific. The convective activities around the low temperatures exhibit no significant difference during this period. These results

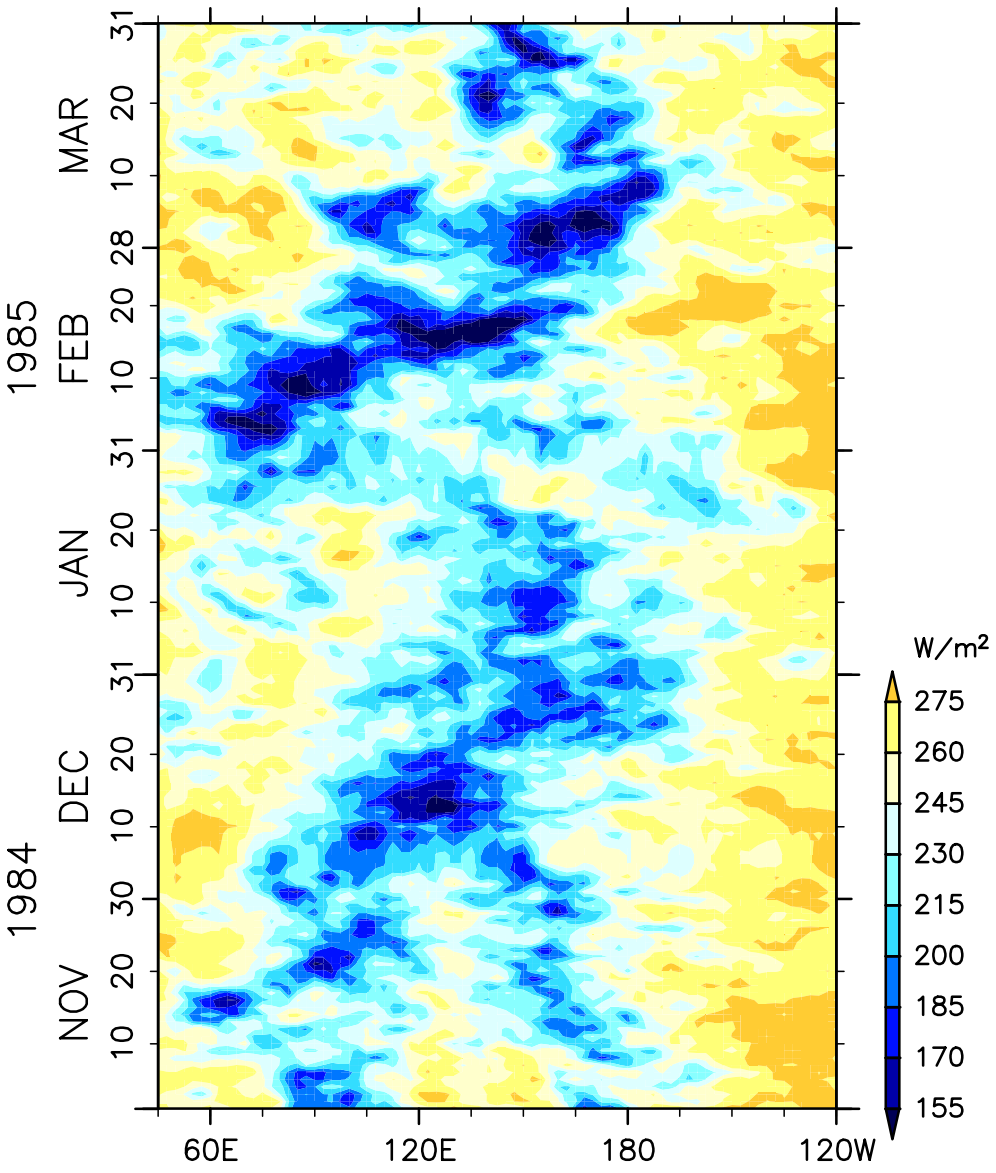


Fig. 4.1 Longitude–time section of the unfiltered OLR ($W\,m^{-2}$) averaged over 5°N–15°S for November–March 1984/85.

are in agreement with the previous study of *Hendon and Salby* [1994], which indicated that the upper-level perturbation associated with the MJO circumnavigates the equatorial belt. Because the low temperatures over both equatorial South America and Africa do not form the horseshoe-shaped structure and are not directly connected to the variability in the convective activities, this paper will not discuss them further.

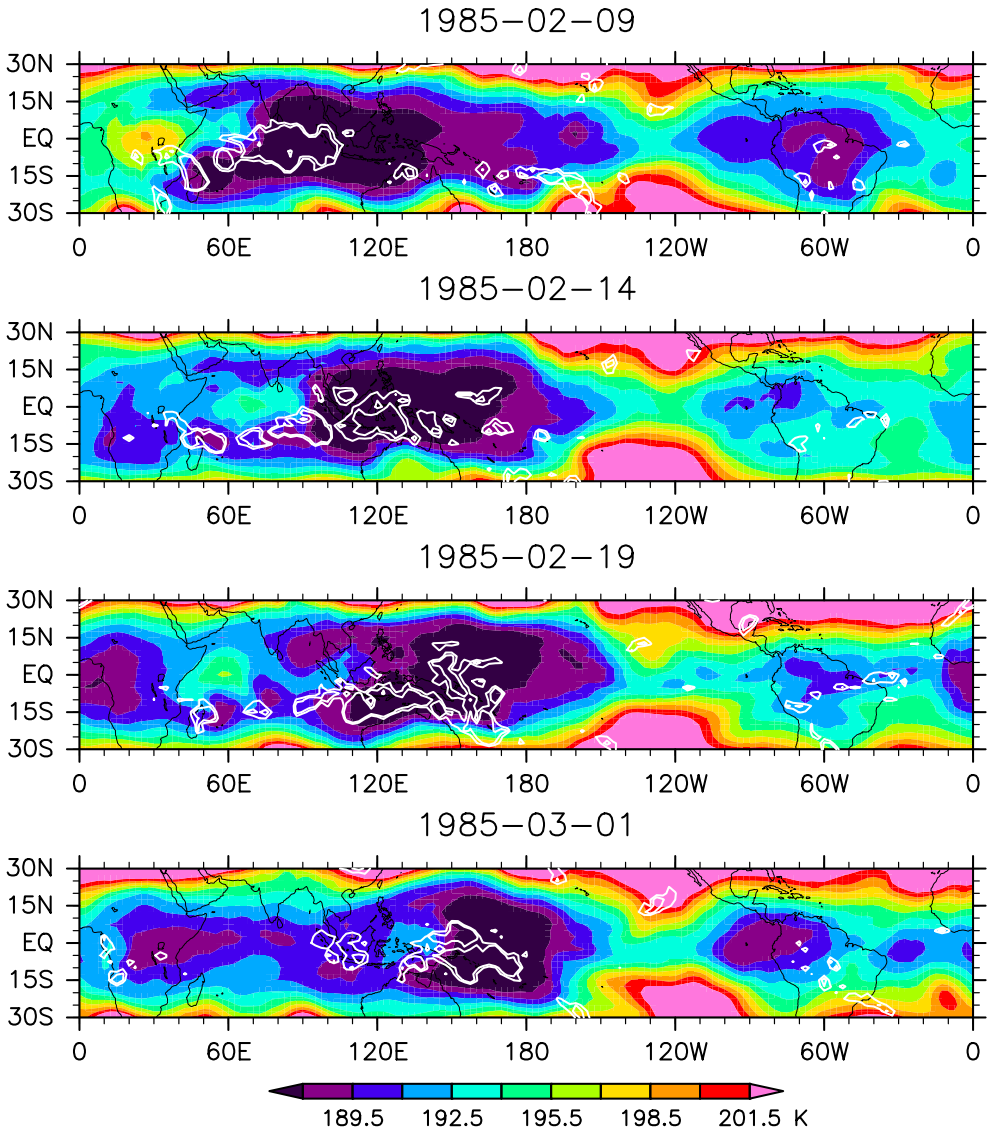


Fig. 4.2 Longitude–latitude sections of the 100-hPa temperature (K, color) and the unfiltered OLR ($W\,m^{-2}$, contour).

## 4.2 Cluster Analysis of ISO Events

### 4.2.1 Selection of ISO Events

The ISO signal is isolated as in *Suzuki and Shiotani* [2008], by space–time filtering OLR to retain only eastward-propagating signals of wavenumbers 1–10 with periods

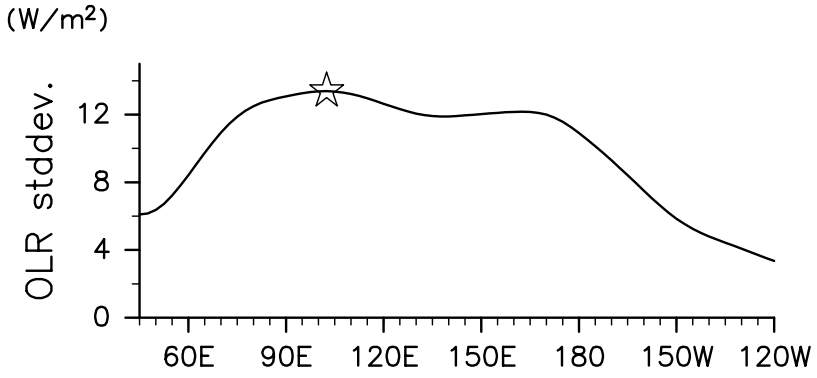


Fig. 4.3 Standard deviation at each longitude of the band-pass-filtered OLR data averaged over 5°N–15°S. The open star indicates the location of maximum standard deviation.

between 23 and 90 days. Figure 4.3 shows the standard deviation of the ISO signal averaged between 5°N and 15°S during the southern summer (November–March). As noted in many previous studies [e.g., *Zhang*, 2005], the convective component of the ISO is most active over the high mean SST warm pool regions of the Indian Ocean around 90°E and the western Pacific around 165°E. The convective component is generally much weaker over the Maritime Continent around 135°E than over the surrounding oceans. The longitude having the maximum standard deviation ($\sigma_{max} =$ 13.382 W/m$^2$), 102.5°E, is used as a reference point.

The time series of the ISO signal averaged over 5°N–15°S at the reference point is used as an index of the ISO. Using a convention similar to those of *Kiladis et al.* [2002] and *Eguchi and Shiotani* [2004], the day having the lowest ISO index value less than $-1\,\sigma_{max}$ ($-13.382$ W/m$^2$) is referred as day 0 (the key day). The key days are searched between November and March and a total of 72 ISO events are selected on the basis of this index in the 32 southern summers. Every event has different features, such as a different propagation speed and intensity, in the observed unfiltered OLR field. Cluster analysis will then be performed according to these features in the next subsection.

### 4.2.2 Cluster Analysis

To categorize the ISO events according to the propagation feature observed in the unfiltered OLR field, cluster analysis is conducted by using the ISO locus, which is selected in the following way. The unfiltered OLR minimum point is first searched around the reference point (102.5°E ± 45.0°E) at the key day. After the key day the OLR minimum point is selected between the ±45° longitude range around the minimum point of the prior day, and before the key day around the minimum point of the following day. The ISO locus is used between day −5 and day 20 because the OLR values are on average low (under 200 W/m$^2$) during this period.

Cluster analysis is performed with Ward's method [*Wilks*, 2011], which is one of the hierarchical clustering methods and defined based on the notion of square error. In Ward's method, at each clustering step, the value of the sum-of-square error is computed for every possible merger of two clusters. The merger which produces the smallest increase in the value of sum-of-square error is taken to be the clustering of this step. This process is repeated in each step until the growth rate of the sum-of-square error suddenly becomes large. Initially, each cluster contains only one object; hence, the value of the sum-of-square error at the beginning is zero.

After the cluster analysis, the total number of 72 ISO events are grouped into five clusters, which contain 20, 20, 18, 12, and 2 events, respectively. No distinct seasonal bias appears in each cluster (not shown). Figure 4.4 displays the ISO locus for the top four clusters (Clusters 1–4). Two major categories are found for the ISO propagation speed, as observed in the unfiltered OLR field. The speeds are estimated by applying a linear least squares fit to the OLR minima points observed in the composite unfiltered OLR field (Figure 4.6), and the correlation coefficients are more than 0.8. The speed of one category is estimated to be about 2.0 m/s (Figure 4.4a and 4.4c for Clusters 1 and 3, respectively) and that of the other is about twice as fast as it to be about 4.5 m/s and 3.4 m/s (Figure 4.4b and 4.4d for Clusters 2 and 4, respectively). As shown in Figure 4.5, most of the events in Clusters 1 and 2 occurred in the La Niña and El

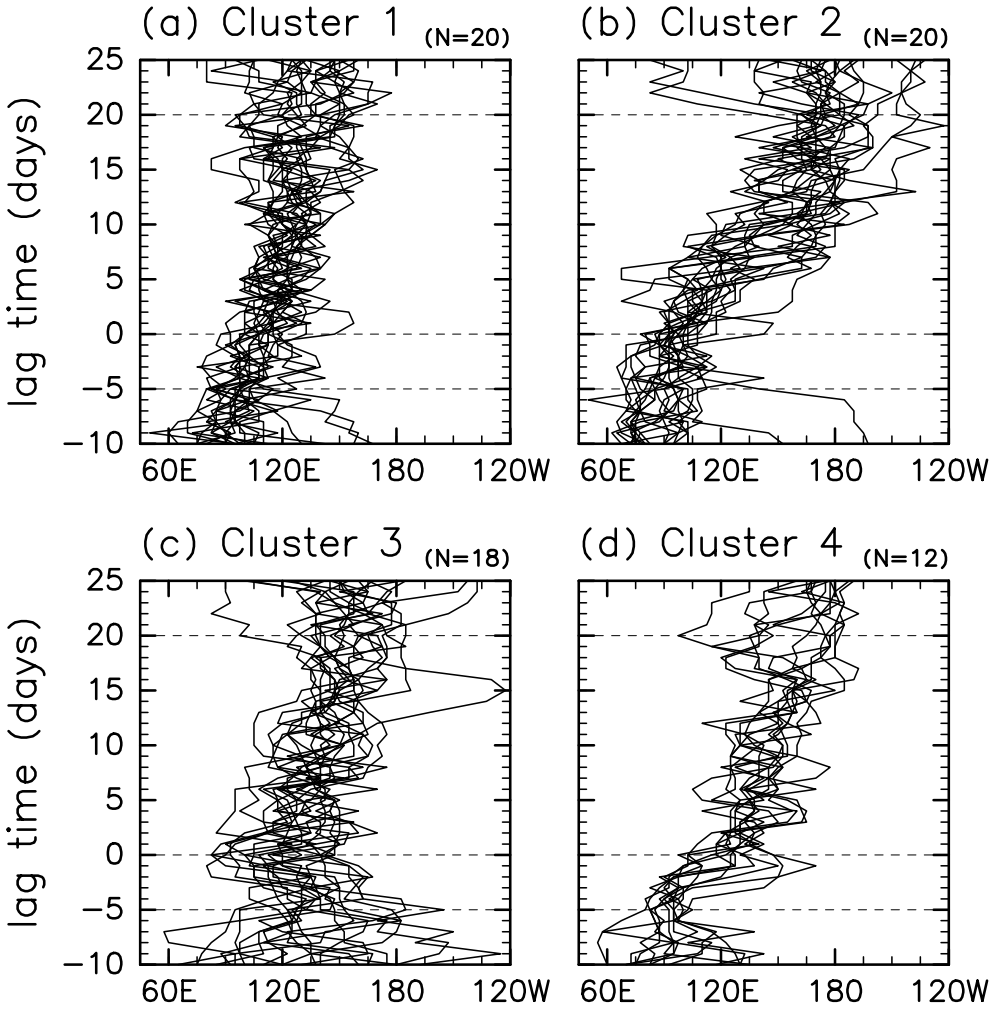


Fig. 4.4 Longitude–time sections of the ISO locus for every event included in (a) Cluster 1, (b) Cluster 2, (c) Cluster 3, and (d) Cluster 4.

Niño periods, respectively, while most of the events in Clusters 3 and 4 occurred in the weak ENSO periods. SST variations over the Pacific would cause the differences in the propagation characteristics, as will be seen in Figure 4.11 and discussed in section 4.3.4.

The ISO signals detected in the unfiltered OLR field for Clusters 1 and 3 propagate eastward until about 120°E and 135°E, respectively, with relatively slow propagation speeds (Figure 4.4a and 4.4c, respectively). Clusters 2 and 4 (Figure 4.4b and 4.4d, respectively) exhibit a faster propagation speed equivalent to the ISO phase speed

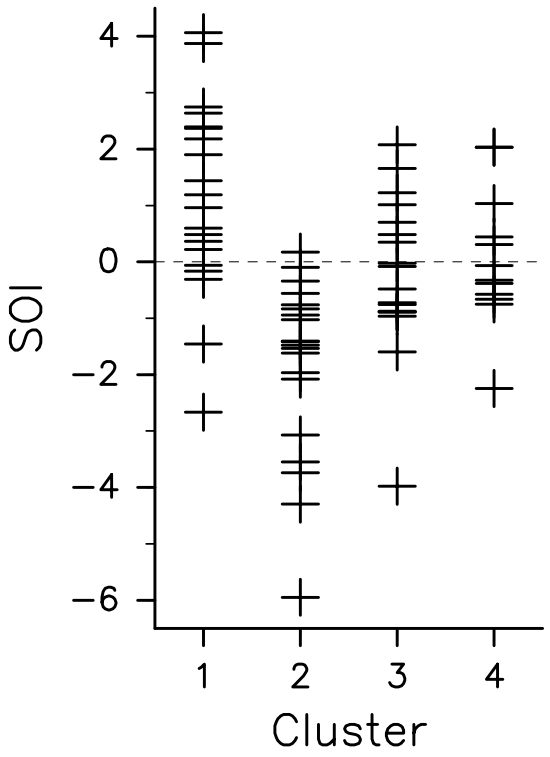


Fig. 4.5 Southern Oscillation Index (SOI) values for the ISO events in each cluster. The SOI values are from a five-month running mean.

which is derived from the anomalous OLR field [e.g., *Hendon and Salby*, 1994]. It is found that each ISO event contains high-frequency variability in the unfiltered OLR field such as eastward-propagating disturbances at the speed of a convectively coupled Kelvin wave and westward-moving disturbances with periods of 2 and 5 days [*Nakazawa*, 1988; *Zhang*, 2005]. Cluster 5 consists of two events in the strong El Niño years and exhibits quasi-stationary fluctuations over the Indian Ocean with weak convective activities (not shown); therefore, the following analyses are focused on the top four clusters.

## 4.3 Characteristics of Each ISO Cluster

### 4.3.1 Convective Activity

Figure 4.6 shows longitude-time sections of the composite band-pass-filtered and unfiltered OLR values averaged between 5°N and 15°S for Clusters 1–4. It is found that the propagation speeds of the convective activities observed in the unfiltered OLR field are much slower in Clusters 1 and 3 compared with those in Clusters 2 and 4, as shown in Figure 4.4. The speed observed in the band-pass-filtered OLR fields are nearly identical among the four clusters.

The quasi-stationary convective area observed in the unfiltered OLR field (colors in Figure 4.6) appears around 135°E in Cluster 3 and to the west of that in Cluster 1 around 120°E as the active convective area in La Niña years occurs over the Indian Ocean and western Pacific in the little farther west of that in normal years [e.g., *Gettelman et al.*, 2001]. Peaks of the convective activities observed in the unfiltered OLR field occur at day 7 in Cluster 1 and at day 6 in Cluster 3, when the ISO signals observed in the band-pass-filtered field (contours) pass over the quasi-stationary areas.

It is found in the unfiltered OLR field (colors in Figure 4.6) that the eastward-propagating convective activities in Cluster 2 penetrate farther eastward into the central Pacific than those in Cluster 4. This difference in the propagation features is also detected in the band-pass-filtered OLR field (contours in Figure 4.6) in agreement with the previous ISO studies in the El Niño southern summers [e.g., *Fink and Speth*, 1997; *Hendon et al.*, 1999]. The convective activities observed in the unfiltered OLR fields for Clusters 2 and 4 each have two peaks in the Indian and Pacific Oceans, respectively. The peaks in Cluster 4 appear around 90°E at day −5 and around 150°E at day 5, while those in Cluster 2 appear around 90°E at day 0 and around 180°E at day 13 with weaker activities than those in Cluster 4.

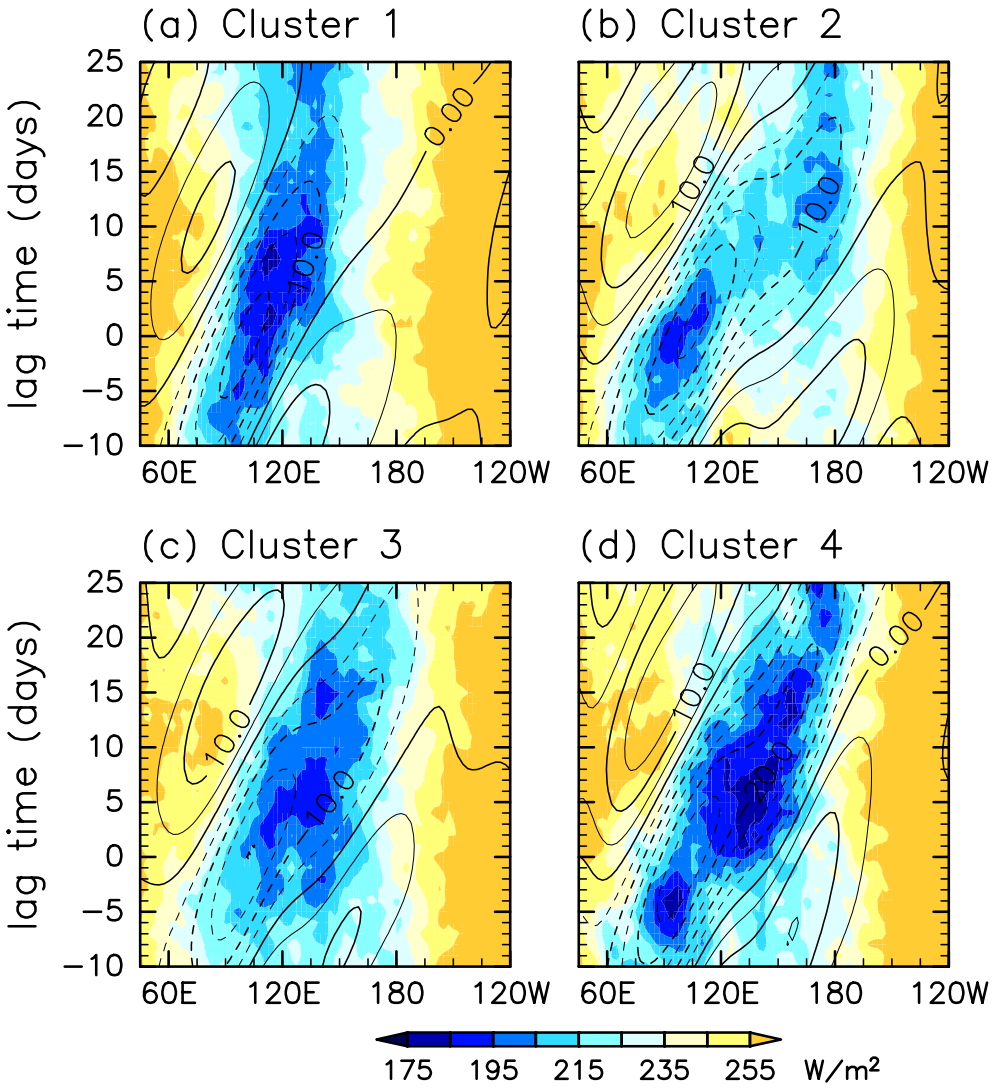


Fig. 4.6 Longitude–time sections of the composite unfiltered OLR (W m$^{-2}$, color) and band-pass-filtered OLR (W m$^{-2}$, contours) averaged over 5°N–15 °S. Contour intervals are 5 W m$^{-2}$.

### 4.3.2 The Horseshoe-shaped Temperature Structure

As seen in Figure 4.2, the low temperatures which form the horseshoe-shaped structure propagate eastward and are accompanied with the eastward-moving active convection. The horseshoe-shaped structure index (HSI-1) is derived by using the daily mean

temperature data at 100 hPa as in *Nishimoto and Shiotani* [2012a] (see details in chapter 3 of this thesis). Because this structure resembles the Matsuno–Gill pattern, the two preliminary indices, HSI-R and HSI-K, are defined to represent these two responses. The two indices are then combined into one index HSI-1 that uses results of EOF analysis applied to HSI-R and HSI-K values. The index HSI-1 projects a positive linear relationship between HSI-R and HSI-K: HSI-1$(x,t) = 1.65\times$HSI-R$(x,t)+1.90\times$ HSI-K$(x+12.5°,t)$. When the HSI-1 value is negative, the temperature field should be representative of the horseshoe-shaped structure. The HSI-1 value is expected to change accordingly in response to heating generated by the convective activities associated with the ISO.

As presented in Figure 4.7, the propagation and intensity features observed in the HSI-1 fields display similarities to those observed in the unfiltered OLR fields. The negative HSI-1 peaks occur about 10°–20° degrees west of the convection centers (open circles). This longitudinal-phase relationship is similar to that observed in the climatological response in and adjacent to monsoon areas [*Nishimoto and Shiotani*, 2012a]. Negative HSI-1 values propagate relatively slowly in Clusters 1 and 3. The peak occurs with strong negative values around 105°E in Cluster 1 and with relatively weak negative values around 120°E in Cluster 3. In contrast, Clusters 2 and 4 exhibit fast-propagating features in the HSI-1 fields. Cluster 4 has strong negative HSI-1 peaks around 90°E and 105°E. A significant peak in Cluster 2 occurs only around 105°E while the unfiltered OLR field has two peaks (Figure 4.6b). However, the correlation coefficient between the HSI-1 and unfiltered OLR values shows significant values for each cluster.

Figure 4.8 shows time series of the composite unfiltered OLR and HSI-1 values between day −10 and day 25 for Clusters 1–4, which are averaged over ±15° degrees of longitude around the minimum locations. The maximum correlation coefficient is 0.92 at a 1-day lag (OLR values preceding HSI-1 values) in Cluster 1, 0.87 at a 2-day lag in Cluster 2, 0.92 at a 1-day lag in Cluster 3, and 0.88 at a 1-day lag in Cluster 4. The 5% significance level is 0.34 when the number of degrees of freedom (N) is 34.

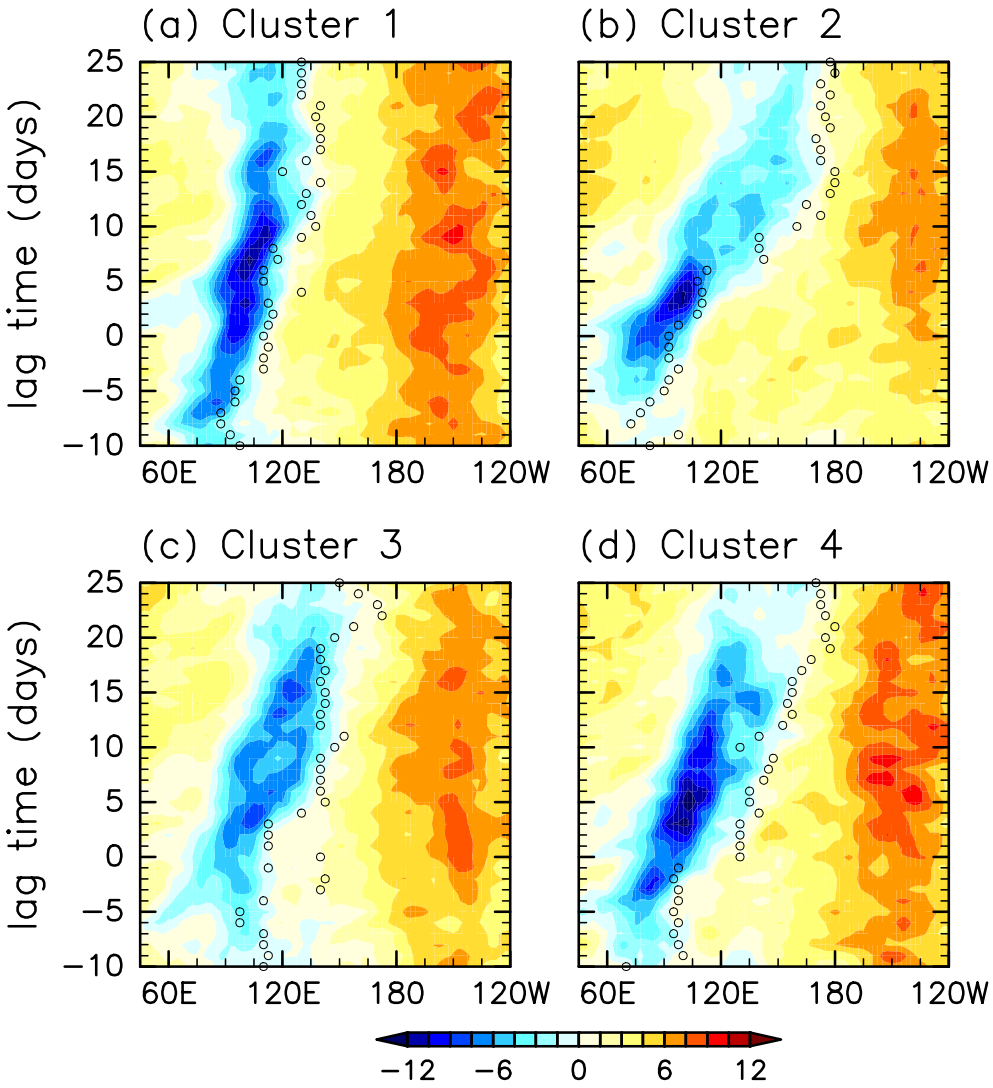


Fig. 4.7 Same as Figure 4.6, but for HSI-1. Open circles show location of the minimum of the unfiltered OLR averaged over 5°N–15°S at each day.

Event-to-event variations in the intensity of the convective activities and horseshoe-shaped temperature structure are also related to each other. Figure 4.9 shows a scatterplot of the OLR and HSI-1 values, which are averaged over ±15° degrees of longitude around the minimum locations and between day −2 and day 2 in each event. Significant correlations are found both for all events ($r$ = 0.61 and N= 72) and for events in each cluster ($r$ = 0.64 and N= 20 in Cluster 1, $r$ = 0.56 and N= 20 in Cluster 2, $r$ = 0.67 and N= 18 in Cluster 3, and $r$ = 0.62 and N= 12 in Cluster 4).

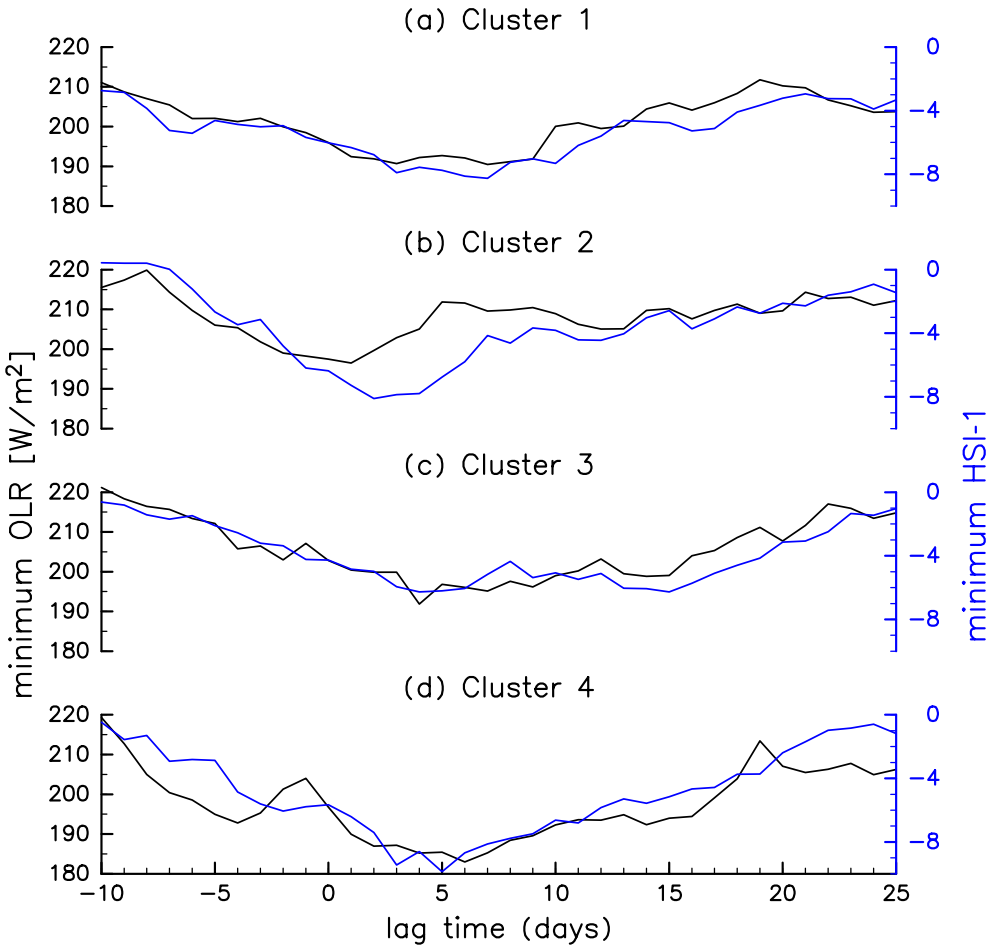


Fig. 4.8 Minima of the composite unfiltered OLR (W $m^{-2}$, black line) and HSI-1 (blue line) time series.

The 5% significance levels are 0.30 at N= 72, 0.44 at N= 20, 0.47 at N= 18, and 0.58 at N= 12. The significant relationships, both in the ISO life cycle and in the event-to-event variation, indicate that the heating generated by the convective activities associated with the ISO could induce the horseshoe-shaped pattern and these could propagate eastward together.

### 4.3.3 The 100-hPa Temperature

Figure 4.10 shows the composite temperature and zonal wind fields at the 100-hPa level averaged over 15°N–15°S for Clusters 1–4. Low temperatures appear about 30°

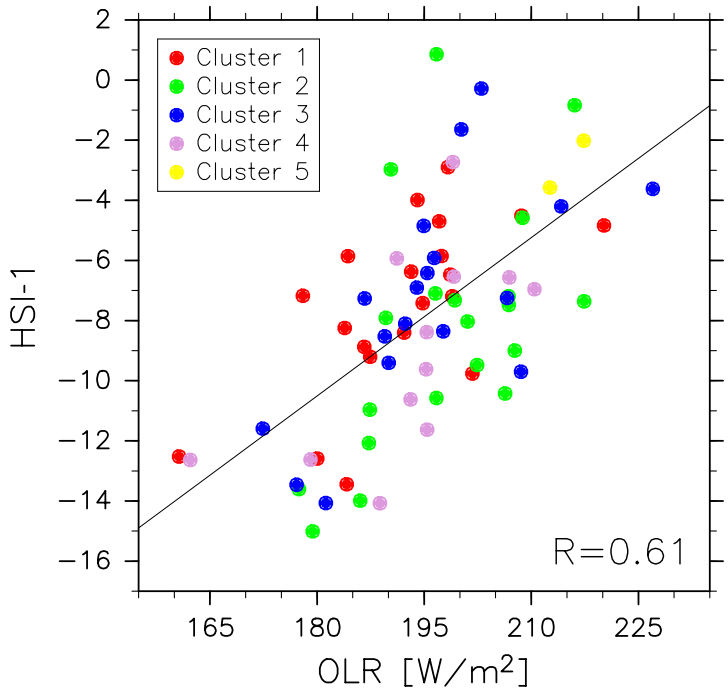


Fig. 4.9 Scatterplots of the unfiltered OLR and HSI-1 values averaged between day −2 and day 2. Red, green, blue, pink, and yellow circles represent Clusters 1–5, respectively.

eastward of the centers of active convection in each cluster, and the easterly wind is located almost over the convection center. Similar relationships have been observed in anomaly fields from the upper-troposphere and lower-stratosphere in previous studies of the ISO [e.g., *Hendon and Salby*, 1994; *Eguchi and Shiotani*, 2004]; temperature anomalies and zonal wind anomalies are observed to be almost in quadrature, which can be regarded as the Kelvin wave response to convective heating.

The 100-hPa temperature minima in the ISO life cycle are significantly correlated with the HSI-1 minima. The correlation coefficient is 0.71 in Cluster 1, 0.50 in Cluster 2, 0.91 in Cluster 3, and 0.83 in Cluster 4. Although the relationship in the event-to-event variation is not large ($r = 0.38$), the low temperatures around the tropical tropopause vary according with the horseshoe-shaped structure at least during the ISO life cycle. As *Hatsushika and Yamazaki* [2003] presented, the horseshoe-shaped temperature structure would effectively dehydrate air in the TTL together with the

accompanying circulations. It is also found that the minimum temperature differs among the clusters. The minimum is 187.7 K at day 4 and 132.5°E in Cluster 1, 188.4 K at day 12 and 180.0°E in Cluster 2, 187.9 K at day 11 and 162.5°E in Cluster 3, and 187.5 K at day 9 and 155.0°E in Cluster 4. *Eguchi and Shiotani* [2004] attributed the occurrence of the cirrus clouds to the low temperatures in the TTL associated with the ISO. These results imply that the dehydration and troposphere-stratosphere exchange processes associated with the ISO would occur at different locations and that the contributions to those processes would be different in the clusters.

### 4.3.4 Sea Surface Temperature

Figure 4.11 shows the composite SST and zonal wind fields at 10 m averaged over 15°N–15°S for Clusters 1–4. The MJO may induce intraseasonal perturbations in SST by disturbing surface fluxes of heat, momentum, and freshwater [e.g., *Zhang*, 1996; *Jones et al.*, 1998; *Zhang and McPhaden*, 2000]. Every cluster has the convective centers (open circles) in between the surface westerly and easterly, and the westerlies are stronger than the easterlies. This situation is similar to that observed in anomalies of SST and surface wind associated with the MJO structure in the equatorial Indian Ocean and western Pacific [*Hendon and Salby*, 1994].

The average SST distributions in Clusters 1 and 2 display the characteristics of those observed during the La Niña and El Niño periods, respectively, and the distributions in Clusters 3 and 4 display the characteristics of those observed during weak ENSO [e.g., *Gettelman et al.*, 2001]. High SSTs in Cluster 1 are confirmed over the western Pacific around 135°E, and low SSTs extend from around the date line to the east. High SSTs in Cluster 2 are broadly distributed between 120°E and 190°E, and low SSTs extend from 240°E to the east. The SSTs in Clusters 3 and 4 are high over 120°E–180°E and are low from 210°E to the east.

The eastward propagation speed of the convective centers in Cluster 4 is faster than that in Cluster 3, as already discussed in sections 4.2.2 and 4.3.1. Although the average SST distributions are observed to be nearly identical between Clusters 3 and

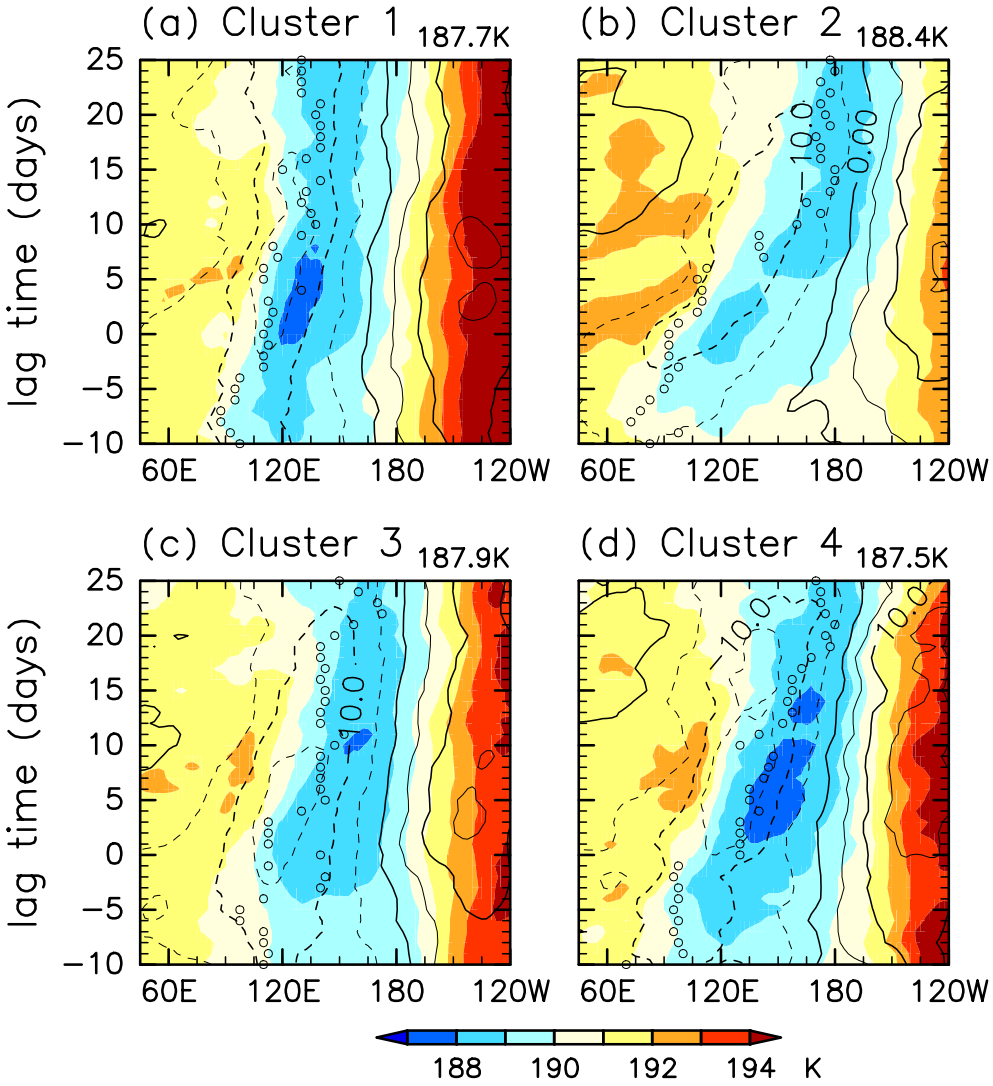


Fig. 4.10 Same as Figure 4.6, but for the tropical temperature (K, color) and zonal wind ($m\,s^{-1}$, contour) at 100 hPa averaged over 15°N–15°S. Contour intervals are 5 $m\,s^{-1}$. Temperature minima are shown above each panel.

4, the SSTs in Cluster 4 are high around 120°E compared to those in Cluster 3. This implies that during the weak ENSO periods the SSTs over the western Pacific would affect the eastward propagation speed of the convective activity associated with the ISO. High SST occurs east of the date line in Cluster 2, and the convective centers propagate over the date line. The farther eastward propagation of the MJO envelope during the El Niño periods is a well-known feature that is observed in the band-pass-

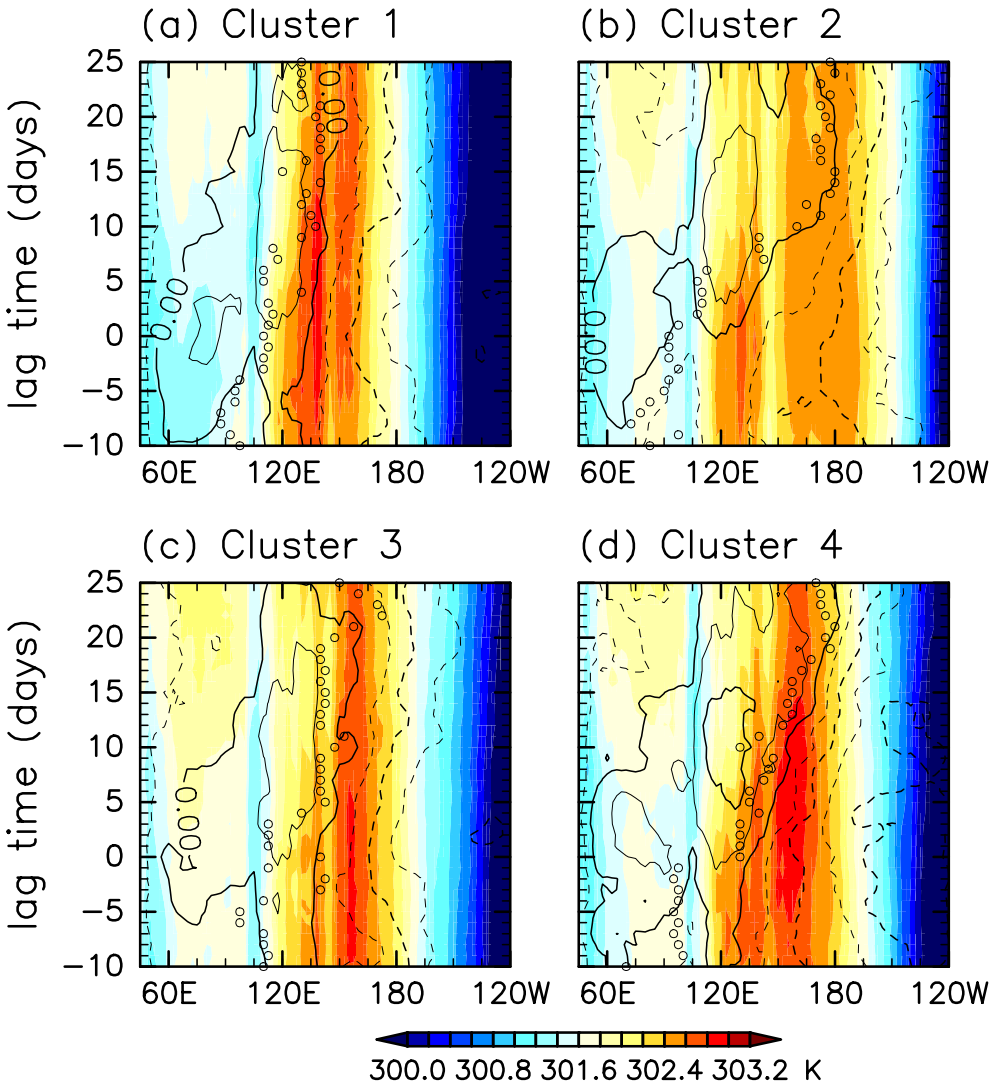


Fig. 4.11 Same as Figure 4.6, but for the SST (K, color) and zonal wind at 10 m (m s$^{-1}$, contour) averaged over 5°N–15°S. Contour intervals are 1.5 m s$^{-1}$.

filtered data [e.g., *Fink and Speth*, 1997; *Hendon et al.*, 1999; *Kessler*, 2001].

## 4.4 Summary

Space–time variations of the tropical convective activity and temperature around the tropical tropopause has been investigated associated with the ISO, such as the MJO, by using NOAA/OLR and ERA-Interim data. In the case study of the 1984/85 south-

ern summer, which is during the weak (normal) ENSO period, various types of the convective propagation features associated with the ISO are observed in the unfiltered OLR field. These convective activities accompany low temperatures to their east in the tropics and to their west in the subtropics around the tropical tropopause. These low temperatures form a horseshoe-shaped structure, which resembles the Matsuno–Gill pattern.

The 72 ISO events that occur during the southern summer from January 1979 to December 2011 were first selected with respect to the time series at the reference point (102.5°E) where variations of the band-pass-filtered OLR averaged over 5°N–15°S are largest. Cluster analysis was then performed with Ward's method by using the locus of the unfiltered OLR minima in the ISO events, and the propagation features were categorized into five clusters, which consist of 20, 20, 18, 12, and 2 events.

Most of the events in Clusters 1 and 2 occur during the La Niña and El Niño periods, respectively, and those in Clusters 3 and 4 during the weak ENSO periods. In association with the ISO, the convective activities observed in the unfiltered OLR field in Clusters 1 and 3 have a relatively slow speed (<2 m/s) and propagate to 120°E and 135°E, respectively. The faster ($\sim$ 4 m/s) convective activities in Clusters 2 and 4 propagate into the central Pacific. The composite SST field reveals the following facts about the convective propagation. During the weak ENSO periods (Clusters 3 and 4), the propagation speed is slow when the SSTs over the western Pacific are relatively low. During the El Niño periods (Cluster 2), as the eastern edge of the warm pool extends over the date line, so does the active convection.

To investigate space–time variability in the horseshoe-shaped temperature structure associated with the ISO, the horseshoe-shaped structure index (HSI-1) was used. The index was defined in *Nishimoto and Shiotani* [2012a]. The composite HSI-1 fields have similar features to those of OLR, located about 10°–20° degrees west of the active convective area. Both the ISO life cycle and event-to-event variation in the HSI-1 values are significantly correlated with those in the unfiltered OLR values. Those results imply that the convective heating associated with the ISO induces the

horseshoe-shaped temperature structure around the tropical tropopause.

Low temperatures at 100 hPa change accordingly with the HSI-1 minima at least in the ISO life cycle. Furthermore, the strength and location of the temperature minima at 100 hPa are different among the ISO clusters. These results could suggest that the different types of the ISO would be different impacts on the troposphere-stratosphere exchange such as the dehydration process depending on their types, considering the previous studies which investigated the possible influence of the the ISO and horseshoe-shaped structure on the troposphere-stratosphere exchange process in the TTL; *Eguchi and Shiotani* [2004] and *Virts and Wallace* [2010] showed that the strong signal of the cirrus clouds appears accompanied with the ISO active convection. *Hatsushika and Yamazaki* [2003] demonstrated that the enhanced upward motion penetrating into the TTL occurs over the active convection region and the circulation characterized by the Matsuno–Gill pattern entrains the tropospheric air parcels. These air parcels then pass over the cold tropopause region several times during the slow ascent in the TTL.

Diagnostic interpretation of reanalysis data [*Kerr-Munslow and Norton*, 2006; *Randel et al.*, 2008] and model simulations [*Boehm and Lee*, 2003; *Norton*, 2006; *Garny et al.*, 2011] revealed that much of the upwelling in the TTL is forced by the dissipation of tropical waves such as the Rossby waves. In Figure 6 of *Eguchi and Shiotani* [2004], the slow ascent is detected over the cold tropopause region in association with the ISO using the ECMWF operational data. Therefore, the upwelling in the TTL may occur over the horseshoe-shaped temperature structure associated with the ISO.

This study clearly revealed the intraseasonal variability in the convective activities and temperatures around the tropical tropopause during the southern summer by employing cluster analysis according to the propagation features of the convective centers. A better understanding of lower troposphere conditions that would induce variations in the propagation features of the convective activities is needed.

# Chapter 5

# Summary

Around the tropical tropopause low temperatures generally occur to the east of tropical active convection around the equator and to the west around 10°N and 10°S, forming a horseshoe-shaped structure. This structure resembles a stationary wave response known as the Matsuno–Gill pattern, which is induced by the heating generated by the convective activities near the equator. However, the relationship with the convective activities and the variability had been unclear. This thesis has performed statistical analyses to reveal the relationship between the horseshoe-shaped temperature structure and convective activities with the intraseasonal, seasonal, and interannual timescales by using contemporary reanalyses from ECMWF and OLR from NOAA.

In chapter 3, an index characterizing the horseshoe-shaped temperature structure was first established to quantitatively capture its variability. By using the monthly mean data this horseshoe-shaped structure index was defined in the Eastern Hemisphere where climatological convective activities occur strongly. Then, the relationship with convective activities in and adjacent to the monsoon regions was investigated with the seasonal and interannual timescales. These are the first direct evidence of the tropopause temperature response to the climatological convective activities.

In chapter 4, the relationship with the eastward-propagating convective activity associated with the intraseasonal oscillation (ISO) was examined. The analysis was

restricted to the southern summer seasons when the eastward-propagating convection is observed predominantly over the Indian and Pacific Ocean. The horseshoe-shaped structure index was derived over 0°E–120°W by using the daily mean data. Cluster analysis was performed according to the eastward propagation features observed in the unfiltered OLR data during the southern summer. This is the first study to present the methodology to categorize ISO propagation types and also the first one to suggest that the different ISOs would cause different impacts on the dehydration and troposphere-stratosphere exchange processes according on their types.

Throughout this thesis it is clearly confirmed that the horseshoe-shaped temperature structure around the tropical tropopause is induced by the heating generated by the convective activities. These results could improve the understanding on the TTL dynamics and, consequently, the troposphere-stratosphere exchange process. The methodologies developed in this thesis are expected to contribute to future tropical studies. The horseshoe-shaped structure index should become a powerful diagnostic tool for investigating the temperature distribution in the tropical tropopause. As the future work, it would be interesting to compare the tropical tropopause temperatures derived from some reanalysis data sets and climate models by using the horseshoe-shaped structure index. The method to categorize the ISOs should be a very helpful to study convectively coupled tropical dynamics. Relationship to the intraseasonal oscillation during the northern summer is an interesting topic for further investigation.

# Publication List

This thesis is based on the two published papers listed below. The chapters 3 and 4 in this thesis mainly consist of the first and second papers, respectively.

1. Nishimoto, E., and M. Shiotani (2012), Seasonal and interannual variability in the temperature structure around the tropical tropopause and its relationship with convective activities, *Journal of Geophysical Research*, *117*(D2), D02,104.

2. Nishimoto, E., and M. Shiotani (2012), Intraseasonal variations in the tropical tropopause temperature revealed by cluster analysis of convective activity, *Journal of Geophysical Research*, *submitted*.

This thesis has been also motivated by the following two published papers. In one paper, the author was in charge of analyses using data obtained by the global positioning system radio-occultation limb-sounding technique of the Constellation Observing System for Meteorology, Ionosphere, and Climate (COSMIC) to detect vertically thin inversion layers over the equator in the Indian Ocean.

3. Nishi, N., E. Nishimoto, H. Hayashi, M. Shiotani, H. Takashima, and T. Tsuda (2010), Quasi-stationary temperature structure in the upper troposphere over the tropical Indian Ocean inferred from radio occultation data, *Journal of Geophysical Research*, *115*(D14), D14,112.

In the other, the author was in charge of analyses using water vapor data observed from the Aura Microwave Limb Sounder (MLS) to display the time series of water vapor mixing ratio in the lower stratosphere.

4. Fujiwara, M., H. Vömel, F. Hasebe, M. Shiotani, S.-Y. Ogino, S. Iwasaki, N. Nishi, T. Shibata, K. Shimizu, E. Nishimoto, J. M. Valverde Canossa, H. B. Selkirk, and S. J. Oltmans (2010), Seasonal to decadal variations of water vapor in the tropical lower stratosphere observed with balloon-borne cryogenic frost point hygrometers, *Journal of Geophysical Research*, *115*(D18), D18,304.

# Acknowledgments

This Ph.D. thesis is a compilation of my work for about five and half years since the spring of 2007 at Laboratory of Atmospheric Environment Information Analysis, Research Institute for Sustainable Humanosphere (RISH), Kyoto University.

Foremost I would like to express my deepest grateful to my main supervisor, Professor Masato Shiotani. He has been a model of scientific excellence and generous mentorship. I deeply appreciate his guidance, support, patience, understanding, and a lot of advices, as a teacher and a researcher.

Thank you to my committee, Professors Shigeo Yoden, Hitoshi Mukougawa, Hirohiko Ishikawa, Takehiko Satomura, and Dr. Noriyuki Nishi, for reading my thesis and providing me with very useful comments and suggestions. Dr. Noriyuki Nishi gave me an opportunity to work on this interesting research topic at the beginning of my graduate school years and has given me constructive comments and suggestions on my works as a supervisor from then on. I would also like to thank Professors Masatomo Fujiwara and Fumio Hasebe of Hokkaido University for giving me their valuable suggestion and advice.

I am also grateful to Prof. Kenshi Takahashi, Dr. Yoko Naito, Dr. Hiroo Hayashi, Dr. Nawo Eguchi, Dr. Hisahiro Takashima, Dr. Junko Suzuki, Ms. Kumi Nakamae, Mr. Tsuyoshi Koshiro, Mr. Kazunari Koishi, and all members in the laboratory for their warm words of encouragement, helpful discussion and advice. In particular, Mr. Tsuyoshi Koshiro took a lot of time to teach me computer skills and to hear my (silly) complaints. I also thank Dr. Junko Suzuki for her constructive comments on my studies and for telling me the interest of the atmospheric researches, which

encourages me to keep studying. Special thanks go to Ms. Akemi Hatano for her helping my study life at the laboratory. Her words always encourage me.

Finally, I am indebted to my husband and parents for their understanding and encouragement to my work. I dedicate this Ph.D. thesis to them!

Data analysis and visualization were done using libraries developed by the GFD-DENNOU Ruby project (http://ruby.gfd-dennou.org/).

# Bibliography

Bergman, J. W., H. H. Hendon, and K. M. Weickmann (2001), Intraseasonal Air-Sea Interactions at the Onset of El Niño, *Journal of Climate*, *14*(8), 1702–1719, doi:10.1175/1520-0442(2001)014⟨1702:IASIAT⟩2.0.CO;2.

Boehm, M. T., and S. Lee (2003), The Implications of Tropical Rossby Waves for Tropical Tropopause Cirrus Formation and for the Equatorial Upwelling of the Brewer–Dobson Circulation, *Journal of the Atmospheric Sciences*, *60*(2), 247–261, doi:10.1175/1520-0469(2003)060⟨0247:TIOTRW⟩2.0.CO;2.

Brewer, A. W. (1949), Evidence for a world circulation provided by the measurements of helium and water vapour distribution in the stratosphere, *Quarterly Journal of the Royal Meteorological Society*, *75*(326), 351–363.

Dee, D. P., et al. (2011), The ERA-Interim reanalysis: configuration and performance of the data assimilation system, *Quarterly Journal of the Royal Meteorological Society*, *137*(656), 553–597.

Dima, I. M., and J. M. Wallace (2007), Structure of the Annual-Mean Equatorial Planetary Waves in the ERA-40 Reanalyses, *Journal of the Atmospheric Sciences*, *64*(8), 2862–2880, doi:10.1175/JAS3985.1.

Dunkerton, T. J. (1995), Evidence of meridional motion in the summer lower stratosphere adjacent to monsoon regions, *Journal of Geophysical Research*, *100*(D8), 16,675–16,688, doi:10.1029/95JD01263.

Eguchi, N., and M. Shiotani (2004), Intraseasonal variations of water vapor and cirrus clouds in the tropical upper troposphere, *Journal of Geophysical Research*, *109*(D12), 1–11, doi:10.1029/2003JD004314.

Fink, A., and P. Speth (1997), Some potential forcing mechanisms of the year-to-year variability of the tropical convection and its intraseasonal (25–70-day) variability, *International Journal of Climatology*, *17*(14), 1513–1534, doi:10.1002/(SICI)1097-0088(19971130)17:14⟨1513::AID-JOC210⟩3.0.CO;2-U.

Fu, Q., C. M. Johanson, J. M. Wallace, and T. Reichler (2006), Enhanced mid-latitude tropospheric warming in satellite measurements., *Science*, *312*(5777), 1179, doi:10.1126/science.1125566.

Fueglistaler, S., and P. H. Haynes (2005), Control of interannual and longer-term variability of stratospheric water vapor, *Journal of Geophysical Research*, *110*, D24,108, doi:10.1029/2005JD006019.

Fujiwara, M., F. Hasebe, M. Shiotani, N. Nishi, H. Vömel, and S. J. Oltmans (2001), Water vapor control at the tropopause by equatorial Kelvin waves observed over the Galápagos, *Geophysical Research Letters*, *28*(16), 3143, doi:10.1029/2001GL013310.

Fujiwara, M., et al. (2009), Cirrus observations in the tropical tropopause layer over the western Pacific, *Journal of Geophysical Research*, *114*, D09,304.

Fujiwara, M., et al. (2010), Seasonal to decadal variations of water vapor in the tropical lower stratosphere observed with balloon-borne cryogenic frost point hygrometers, *Journal of Geophysical Research*, *115*(D18), D18,304, doi:10.1029/2010JD014179.

Garny, H., M. Dameris, W. Randel, G. E. Bodeker, and R. Deckert (2011), Dynamically Forced Increase of Tropical Upwelling in the Lower Stratosphere, *Journal of the Atmospheric Sciences*, *68*(6), 1214–1233, doi:10.1175/2011JAS3701.1.

Gettelman, A. (2004), Impact of monsoon circulations on the upper troposphere and lower stratosphere, *Journal of Geophysical Research*, *109*(D22), D22,101, doi:10.1029/2004JD004878.

Gettelman, A., W. J. Randel, S. Massie, F. Wu, W. G. Read, and J. M. Russell (2001), El Niño as a Natural Experiment for Studying the Tropical Tropopause Region, *Journal of Climate*, *14*(16), 3375–3392.

Gill, A. E. (1980), Some simple solutions for heat-induced tropical circulation, *Quarterly Journal of the Royal Meteorological Society*, *106*(449), 447–462, doi:10.1002/qj.49710644905.

Gruber, A., and A. F. Krueger (1984), The Status of the NOAA Outgoing Longwave Radiation Data Set, *Bulletin of the American Meteorological Society*, *65*(9), 958–962.

Gutzler, D. (1991), Interannual fluctuations of intraseasonal variance of near-equatorial zonal winds, *Journal of Geophysical Research*, *96*, 3173–3185.

Hatsushika, H., and K. Yamazaki (2001), Interannual variations of temperature and vertical motion at the tropical tropopause associated with ENSO, *Geophysical Research Letters*, *28*(15), 2891–2894, doi:10.1029/2001GL012977.

Hatsushika, H., and K. Yamazaki (2003), Stratospheric drain over Indonesia and dehydration within the tropical tropopause layer diagnosed by air parcel trajectories, *Journal of Geophysical Research*, *108*, 4610, doi:10.1029/2002JD002986.

Hayes, S. P., L. J. Mangum, J. Picaut, A. Sumi, and K. Takeuchi (1991), TOGA-TAO: A Moored Array for Real-time Measurements in the Tropical Pacific Ocean, *Bulletin of the American Meteorological Society*, *72*(3), 339–347.

Hendon, H. H., and M. L. Salby (1994), The Life Cycle of the Madden–Julian Oscillation, *Journal of the Atmospheric Sciences*, *51*(15), 2225–2237, doi:10.1175/

1520-0469(1994)051⟨2225:TLCOTM⟩2.0.CO;2.

Hendon, H. H., C. Zhang, and J. D. Glick (1999), Interannual Variation of the Madden–Julian Oscillation during Austral Summer, *Journal of Climate*, *12*(8), 2538–2550, doi:10.1175/1520-0442(1999)012⟨2538:IVOTMJ⟩2.0.CO;2.

Highwood, E. J., and B. J. Hoskins (1998), The tropical tropopause, *Quarterly Journal of the Royal Meteorological Society*, *124*(549), 1579–1604, doi:10.1002/qj.49712454911.

Holton, J. R., and A. Gettelman (2001), Horizontal transport and the dehydration of the stratosphere, *Geophysical Research Letters*, *28*(14), 2799, doi:10.1029/2001GL013148.

Hoskins, B. J., and B. Wang (2006), The Asian Monsoon, Chapter 9 Large-Scale Atmospheric Dynamics, *Springer, Chichester, UK.*, *edited by*, pp. 378.

Hung, C.-W., and M. Yanai (2004), Factors contributing to the onset of the Australian summer monsoon, *Quarterly Journal of the Royal Meteorological Society*, *130*(597), 739–758.

Immler, F., K. Krüger, M. Fujiwara, G. Verver, M. Rex, and O. Schrems (2008), Correlation between equatorial Kelvin waves and the occurrence of extremely thin ice clouds at the tropical tropopause, *Atmospheric Chemistry and Physics*, *8*(14), 4019–4026, doi:10.5194/acp-8-4019-2008.

Jensen, E. (2004), Transport and freeze-drying in the tropical tropopause layer, *Journal of Geophysical Research*, *109*(D2), D02,207, doi:10.1029/2003JD004022.

Jones, C., D. E. Waliser, and C. Gautier (1998), The Influence of the Madden–Julian Oscillation on Ocean Surface Heat Fluxes and Sea Surface Temperature, *Journal of Climate*, *11*(5), 1057–1072, doi:10.1175/1520-0442(1998)011⟨1057:TIOTMJ⟩2.0.CO;2.

Kawamura, R., T. Matsuura, and S. Iizuka (2001a), Role of equatorially asymmetric sea surface temperature anomalies in the Indian Ocean in the Asian summer monsoon and El Niño–Southern Oscillation coupling, *Journal of Geophysical Research*, *106*(D5), 4681–4693, doi:10.1029/2000JD900610.

Kawamura, R., T. Matsuura, and S. Iizuka (2001b), Interannual atmosphere–ocean variations in the tropical western North Pacific relevant to the Asian summer monsoon-ENSO coupling, *Journal of the Meteorological Society of Japan*, *79*(4), 883–898.

Kerr-Munslow, A. M., and W. A. Norton (2006), Tropical Wave Driving of the Annual Cycle in Tropical Tropopause Temperatures. Part I: ECMWF Analyses, *Journal of the Atmospheric Sciences*, *63*(5), 1410–1419.

Kessler, W. S. (2001), EOF Representations of the Madden–Julian Oscillation and Its Connection with ENSO, *Journal of Climate*, *14*(13), 3055–3061, doi:10.1175/1520-0442(2001)014⟨3055:EROTMJ⟩2.0.CO;2.

Kiladis, G. N., K. H. Straub, G. C. Reid, and K. S. Gage (2001), Aspects of interannual and intraseasonal variability of the tropopause and lower stratosphere, *Quarterly Journal of the Royal Meteorological Society*, *127*(576), 1961–1983, doi:10.1002/qj.49712757606.

Kiladis, G. N., D. J. Seidel, and K. H. Straub (2002), Variability of the tropical tropopause, *SPARC Newsletter*, *18*, 18–22.

Kiladis, G. N., K. H. Straub, and P. T. Haertel (2005), Zonal and Vertical Structure of the Madden–Julian Oscillation, *Journal of the Atmospheric Sciences*, *62*(8), 2790–2809, doi:10.1175/JAS3520.1.

Kley, D., J. M. R. III, and C. Phillips (Eds.) (2000), *SPARC assessment of upper tropospheric and lower stratospheric water vapor*, WCRI 113, 312 pp., World Meteorol. Organ.

Konopka, P., J.-U. Grooß, F. Plöger, and R. Müller (2009), Annual cycle of horizontal in-mixing into the lower tropical stratosphere, *Journal of Geophysical Research*, *114*(D19), 1–7, doi:10.1029/2009JD011955.

Konopka, P., J.-U. Grooß, G. Günther, F. Ploeger, R. Pommrich, R. Müller, and N. Livesey (2010), Annual cycle of ozone at and above the tropical tropopause: observations versus simulations with the Chemical Lagrangian Model of the Stratosphere (CLaMS), *Atmospheric Chemistry and Physics*, *10*(1), 121–132, doi: 10.5194/acp-10-121-2010.

Madden, R. A., and P. R. Julian (1972), Description of Global-Scale Circulation Cells in the Tropics with a 40–50 Day Period, *Journal of the Atmospheric Sciences*, *29*(6), 1109–1123, doi:10.1175/1520-0469(1972)029⟨1109:DOGSCC⟩2.0.CO;2.

Madden, R. A., and P. R. Julian (1994), Observations of the 40–50-Day Tropical Oscillation—A Review, *Monthly Weather Review*, *122*(5), 814–837.

Matsuno, T. (1966), Quasi-Geostrophic Motions in the Equatorial Area, *Journal of the Meteorological Society of Japan*, *44*(1), 25–43.

Mote, P. W., et al. (1996), An atmospheric tape recorder: The imprint of tropical tropopause temperatures on stratospheric water vapor, *Journal of Geophysical Research*, *101*(D2), 3989–4006, doi:10.1029/95JD03422.

Murakami, T., and J. Matsumoto (1994), Summer monsoon over the Asian continent and western North Pacific, *Journal of the Meteorological Society of Japan*, *72*(5), 719–745.

Nakazawa, T. (1988), Tropical Super Clusters within Intraseasonal Variations over the Western Pacific, *Journal of the Meteorological Society of Japan*, *66*(6), 823–839.

Newell, R. E., and S. Gould-Stewart (1981), A Stratospheric Fountain?, *Journal of the Atmospheric Sciences*, *38*(12), 2789–2796.

Nishi, N., E. Nishimoto, H. Hayashi, M. Shiotani, H. Takashima, and T. Tsuda (2010), Quasi-stationary temperature structure in the upper troposphere over the tropical Indian Ocean inferred from radio occultation data, *Journal of Geophysical Research*, *115*(D14), D14,112, doi:10.1029/2009JD012857.

Nishimoto, E., and M. Shiotani (2012a), Seasonal and interannual variability in the temperature structure around the tropical tropopause and its relationship with convective activities, *Journal of Geophysical Research*, *117*(D2), D02,104, doi:10.1029/2011JD016936.

Nishimoto, E., and M. Shiotani (2012b), Intraseasonal variations in the tropical tropopause temperature revealed by cluster analysis of convective activity, *Journal of Geophysical Research*, *submitted*.

Niwano, M. (2003), Seasonal and QBO variations of ascent rate in the tropical lower stratosphere as inferred from UARS HALOE trace gas data, *Journal of Geophysical Research*, *108*(D24), doi:10.1029/2003JD003871.

Norton, W. A. (2006), Tropical Wave Driving of the Annual Cycle in Tropical Tropopause Temperatures. Part II: Model Results, *Journal of the Atmospheric Sciences*, *63*(5), 1420–1431.

Oltmans, S. J., H. Vömel, D. J. Hofmann, K. H. Rosenlof, and D. Kley (2000), The increase in stratospheric water vapor from balloonborne, frostpoint hygrometer measurements at Washington, D.C., and Boulder, Colorado, *Geophysical Research Letters*, *27*(21), 3453, doi:10.1029/2000GL012133.

Park, M. (2004), Seasonal variation of methane, water vapor, and nitrogen oxides near the tropopause: Satellite observations and model simulations, *Journal of Geophysical Research*, *109*(D3), 1–16, doi:10.1029/2003JD003706.

Park, M., W. J. Randel, A. Gettelman, S. T. Massie, and J. H. Jiang (2007), Transport above the Asian summer monsoon anticyclone inferred from Aura Microwave Limb

Sounder tracers, *Journal of Geophysical Research*, *112*(D16), D16,309, doi:10.1029/2006JD008294.

Park, M., W. J. Randel, L. K. Emmons, P. F. Bernath, K. A. Walker, and C. D. Boone (2008), Chemical isolation in the Asian monsoon anticyclone observed in Atmospheric Chemistry Experiment (ACE-FTS) data, *Atmospheric Chemistry and Physics*, *8*(3), 757–764, doi:10.5194/acp-8-757-2008.

Park, M., W. J. Randel, L. K. Emmons, and N. J. Livesey (2009), Transport pathways of carbon monoxide in the Asian summer monsoon diagnosed from Model of Ozone and Related Tracers (MOZART), *Journal of Geophysical Research*, *114*(D8), 1–11, doi:10.1029/2008JD010621.

Ploeger, F., P. Konopka, G. Günther, J.-U. Grooß, and R. Müller (2010), Impact of the vertical velocity scheme on modeling transport in the tropical tropopause layer, *Journal of Geophysical Research*, *115*(D3), 1–14, doi:10.1029/2009JD012023.

Randel, W. J., and M. Park (2006), Deep convective influence on the Asian summer monsoon anticyclone and associated tracer variability observed with Atmospheric Infrared Sounder (AIRS), *Journal of Geophysical Research*, *111*(D12), D12,314, doi:10.1029/2005JD006490.

Randel, W. J., and F. Wu (2010), The Polar Summer Tropopause Inversion Layer, *Journal of the Atmospheric Sciences*, *67*(8), 2572–2581, doi:10.1175/2010JAS3430.1.

Randel, W. J., F. Wu, A. Gettelman, J. M. Russell, J. M. Zawodny, and S. J. Oltmans (2001), Seasonal variation of water vapor in the lower stratosphere observed in Halogen Occultation Experiment data, *Journal of Geophysical Research*, *106*(D13), 14,313–14,325, doi:10.1029/2001JD900048.

Randel, W. J., F. Wu, S. J. Oltmans, K. Rosenlof, and G. E. Nedoluha (2004), Interannual Changes of Stratospheric Water Vapor and Correlations with Tropical

Tropopause Temperatures, *Journal of the Atmospheric Sciences*, *61*(17), 2133–2148, doi:10.1175/1520-0469(2004)061⟨2133:ICOSWV⟩2.0.CO;2.

Randel, W. J., R. Garcia, and F. Wu (2008), Dynamical Balances and Tropical Stratospheric Upwelling, *Journal of the Atmospheric Sciences*, *65*(11), 3584–3595, doi:10.1175/2008JAS2756.1.

Rosenlof, K. H., et al. (2001), Stratospheric water vapor increases over the past half-century, *Geophysical Research Letters*, *28*(7), 1195, doi:10.1029/2000GL012502.

Roundy, P. E. (2012a), Tracking and prediction of large-scale organized tropical convection by spectrally focused two-step space-time EOF analysis, *Quarterly Journal of the Royal Meteorological Society*, *138*(665), 919–931, doi:10.1002/qj.962.

Roundy, P. E. (2012b), Observed Structure of Convectively Coupled Waves as a Function of Equivalent Depth: Kelvin Waves and the MaddenJulian Oscillation, *Journal of the Atmospheric Sciences*, *69*(7), 2097–2106, doi:10.1175/JAS-D-12-03.1.

Roundy, P. E. (2012c), The Spectrum of Convectively Coupled Kelvin Waves and the Madden–Julian Oscillation in Regions of Low-Level Easterly and Westerly Background Flow, *Journal of the Atmospheric Sciences*, *69*(7), 2107–2111, doi:10.1175/JAS-D-12-060.1.

Scaife, A. A., N. Butchart, D. R. Jackson, and R. Swinbank (2003), Can changes in ENSO activity help to explain increasing stratospheric water vapor?, *Geophysical Research Letters*, *30*(17), 1880, doi:10.1029/2003GL017591.

Scherer, M., H. Vömel, S. Fueglistaler, S. J. Oltmans, and J. Staehelin (2008), Trends and variability of midlatitude stratospheric water vapour deduced from the re-evaluated Boulder balloon series and HALOE, *Atmospheric Chemistry and Physics*, *8*(5), 1391–1402, doi:10.5194/acp-8-1391-2008.

Schuck, T. J., C. a. M. Brenninkmeijer, a. K. Baker, F. Slemr, P. F. J. V. Velthoven,

and A. Zahn (2010), Greenhouse gas relationships in the Indian summer monsoon plume measured by the CARIBIC passenger aircraft, *Atmospheric Chemistry and Physics Discussions*, *10*(2), 2031–2087, doi:10.5194/acpd-10-2031-2010.

Seidel, D. J., R. J. Ross, J. K. Angell, and G. C. Reid (2001), Climatological characteristics of the tropical tropopause as revealed by radiosondes, *Journal of Geophysical Research*, *106*(D8), 7857–7878, doi:10.1029/2000JD900837.

Sherwood, S., and A. Dessler (2000), On the control of stratospheric humidity, *Geophysical Research Letters*, *27*(16), 2513–2516.

Suzuki, J., and M. Shiotani (2008), Space-time variability of equatorial Kelvin waves and intraseasonal oscillations around the tropical tropopause, *Journal of Geophysical Research*, *113*(D16), D16,110, doi:10.1029/2007JD009456.

Tian, B., D. E. Waliser, E. J. Fetzer, B. H. Lambrigtsen, Y. L. Yung, and B. Wang (2006), Vertical Moist Thermodynamic Structure and Spatial–Temporal Evolution of the MJO in AIRS Observations, *Journal of the Atmospheric Sciences*, *63*(10), 2462–2485, doi:10.1175/JAS3782.1.

Tian, B., D. E. Waliser, E. J. Fetzer, and Y. L. Yung (2010), Vertical Moist Thermodynamic Structure of the Madden–Julian Oscillation in Atmospheric Infrared Sounder Retrievals: An Update and a Comparison to ECMWF Interim Re-Analysis, *Monthly Weather Review*, *138*(12), 4576–4582, doi:10.1175/2010MWR3486.1.

Uppala, S. M., et al. (2005), The ERA-40 re-analysis, *Quarterly Journal of the Royal Meteorological Society*, *131*(612), 2961–3012, doi:10.1256/qj.04.176.

Virts, K. S., and J. M. Wallace (2010), Annual, Interannual, and Intraseasonal Variability of Tropical Tropopause Transition Layer Cirrus, *Journal of the Atmospheric Sciences*, *67*(10), 3097–3112, doi:10.1175/2010JAS3413.1.

Wheeler, M. C., and H. H. Hendon (2004), An All-Season Real-Time Multi-

variate MJO Index: Development of an Index for Monitoring and Prediction, *Monthly Weather Review*, *132*(8), 1917–1932, doi:10.1175/1520-0493(2004)132⟨1917:AARMMI⟩2.0.CO;2.

Wilks, D. S. (2011), *Statistical methods in the atmospheric sciences*, vol. 100, Academic Press.

Yulaeva, E., and J. M. Wallace (1994), The Signature of ENSO in Global Temperature and Precipitation Fields Derived from the Microwave Sounding Unit, *Journal of Climate*, *7*(11), 1719–1736.

Zhang, C. (1996), Atmospheric Intraseasonal Variability at the Surface in the Tropical Western Pacific Ocean, *Journal of the Atmospheric Sciences*, *53*(5), 739–758, doi:10.1175/1520-0469(1996)053⟨0739:AIVATS⟩2.0.CO;2.

Zhang, C. (2005), Madden–Julian Oscillation, *Reviews of Geophysics*, *43*(2), 1–36, doi:10.1029/2004RG000158.

Zhang, C., and M. J. McPhaden (2000), Intraseasonal Surface Cooling in the Equatorial Western Pacific, *Journal of Climate*, *13*(13), 2261–2276, doi:10.1175/1520-0442(2000)013⟨2261:ISCITE⟩2.0.CO;2.